学位申請論文

伊東 裕

Thesis

Superconductivity Transition of κ-Type BEDT-TTF Salts under Magnetic Field

Hiroshi Ito

Department of Physics
Faculty of Science
Kyoto University

Contents

Contents

Chapter 1

Introduction

1.1 Superconductivity of κ-(BEDT-TTF)$_2$X

More than 50 kinds of organic superconductors have been synthesized since the discovery of the superconductivity transition in the organic salt (TMTSF)$_2$PF$_6$ at 0.9 K under pressure of 1.2 GPa reported in 1980 [1]. Among them, the salts based on BEDT-TTF, where BEDT-TTF is bis(ethylenedithio)tetrathiafulvalene (Fig. 1.1), have attracted much attention due to the rich variety of materials and the high superconductivity transition temperature (T_c) [2]. The first BEDT-TTF based organic superconductor, (BEDT-TTF)$_2$ReO$_4$, with the transition temperature T_c of 2 K was found under pressure of 0.4 GPa in 1983 [2]. Soon after this, the ambient pressure superconductor β-(BEDT-TTF)$_2$I$_3$ was discovered [3]. The T_c of this salt was 1.4 K at ambient pressure, but it was raised up to 8.1 K by applying pressure of 0.1 GPa [4,5]. The BEDT-TTF organic salt exhibits metallic conduction due to the charge transfer between BEDT-TTF molecules and counter anions, such as ReO$_4^-$ and I$_3^-$ The BEDT-TTF molecules aggregate together to make stacks working as conducting layers. Due to the two-dimensionality (2D), the BEDT-TTF charge transfer salts are free from the Peierls instability which hinders the electrical conduction in the one-dimensional metals.
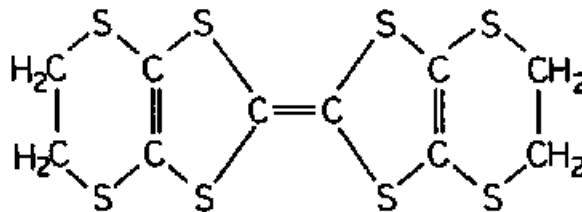

Figure 1.1: BEDT-TTF molecule

The T_c of the organic salts exceeded 10 K through the discovery of κ-(BEDT-TTF)$_2$Cu(NCS)$_2$ in 1988 [6]. In this salt, orthogonally aligned BEDT-TTF dimers form the 2D conducting layer which is sandwiched by the polymeric anion layers of [Cu(NCS)$_2^-$]$_n$. By decreasing the temperature (T), the resistivity increases after showing a slight minimum around 270 K and yields a peak around 90 K, where the resistivity is 3~4 times larger than the room-temperature value as shown in Fig. 1.2(a). After that the resistivity decreases rapidly, in a manner almost characterized by the T^2-law, until T_c of 10.4 K (the midpoint of the resistivity change). The temperature width of the resistive transition between the onset and offset is 1 K even in the case of the best quality sample. The onset temperature of the magnetic transition is 9~9.5 K, which is close to the offset temperature of the resistive transition. The magnetization in the normal state shows no anomaly at 90 K, although it shows decrease below 60 K.

Williams *et al.* demonstrated the usefulness of the ligand N(CN)$_2$ to obtain superconductors of higher T_c, and prepared κ-(BEDT-TTF)$_2$Cu[N(CN)$_2$]Br having T_c of 11.6 K in 1990 [7]. This salt has also layered crystal structure. It shows the similar temperature dependence of the resistivity, although the peak value of resistivity is smaller than that of κ-(BEDT-TTF)$_2$Cu(NCS)$_2$, about 1.2~1.5 times of the room-temperature value as shown in Fig. 1.2(b). The resistive supercon-ductivity transition is sharper than that for κ-(BEDT-TTF)$_2$Cu(NCS)$_2$: the transition width is ~0.5 K. The relation between the magnetic transition temperature and the offset of the resistive transition holds also for this salt. The behavior of the magnetization in the normal state is similar to κ-(BEDT-TTF)$_2$Cu(NCS)$_2$.

Succeedingly, κ-(BEDT-TTF)$_2$Cu[N(CN)$_2$]Cl was found to be superconducting at 12.5 K under pressure above 30 MPa ,which is the highest transition temperature among the organic supercon-ductors to date [8]. This salt is insulating at ambient pressure, as shown in Fig. 1.2(c). With the decrease of temperature, the resistivity continues to increase during cooling. In Fig. 1.2(c), the resistivity decreases slightly below 12 K, which is ascribed to a weak trace of superconduc-tivity even at ambient pressure. However, this salt shows weak ferromagnetism below 22 K [9]. Recently the antiferromagnetic transition at 27 K is claimed and the ferromagnetic transition at 22 K is ascribed to the canting of antiferromagnetically ordered spins [10,11]. Around the critical pressure region below 100 MPa, the superconductivity transition shows the reentrant behavior [12]. The superconductivity state is stable only in the restricted temperature region below T_{c1}~13
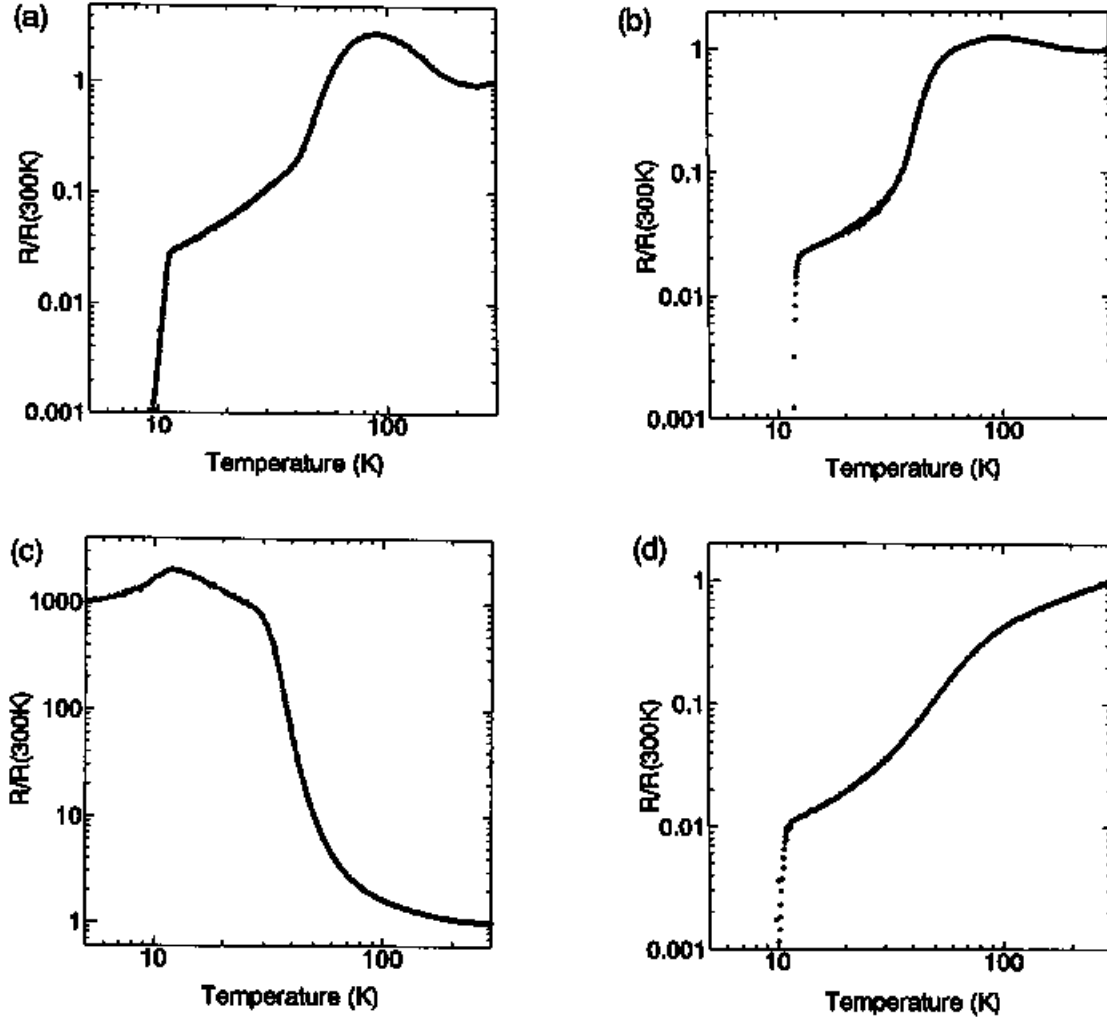
Figure 1.2: The over-all temperature dependences of the resistivity from room temperature to T_c scaled by the resistivity at 300 K, for κ-type BEDT-TTF salts, κ-(BEDT-TTF)$_2$Cu(NCS)$_2$ (a), κ-(BEDT-TTF)$_2$Cu[N(CN)$_2$]Br (b), κ-(BEDT-TTF)$_2$Cu[N(CN)$_2$]Cl (c) and κ-(BEDT-TTF)$_2$CuCN[N(CN)$_2$] (d). The temperature and resistivity are given in the logarithmic scales.

K and above $T_{c2} \sim 6.7$ K. This reentrant transition is influenced by the history of the change in temperature and applied magnetic field [13].

The correlation between the T_c and the effective volume of one carrier in a unit cell has been pointed out [14]. On the basis of the effective volume consideration, it is advantageous to use 2D and thin anion layer composed of large anion unit, and furthermore, the salt should have small thermal contraction in order to have high T_c. Therefore attention has been directed to use CN$^-$ instead of Br$^-$ or Cl$^-$, since CN$^-$ is a thinner and longer anion than those. Along this idea, κ-(BEDT-TTF)$_2$CuCN[N(CN)$_2$] was synthesized in 1991, although the transition temperature is 10.7 K which falls between those of κ-(BEDT-TTF)$_2$Cu(NCS)$_2$ and κ-(BEDT-TTF)$_2$Cu[N(CN)$_2$]Br

5
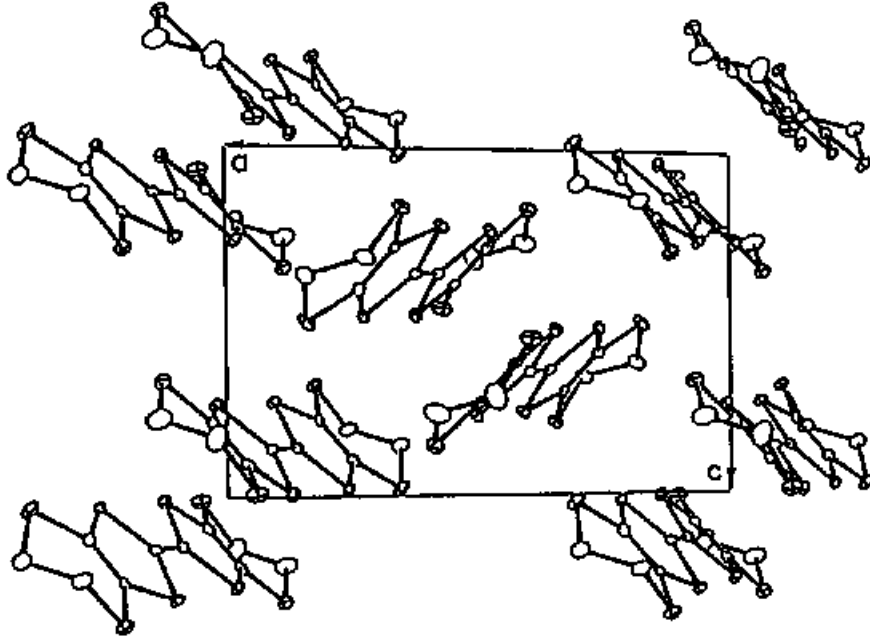
Figure 1.3: The κ-type arrangement of BEDT-TTF molecules observed from the direction orthogonal to the 2D layer.

[15]. The transition behavior is similar to the other salts, although this salt shows monotonous resistivity decrease from room temperature to T_c, as shown in Fig. 1.2(d).

1.2 Electronic Structure of κ-Type BEDT-TTF Salt

All of the four kinds of BEDT-TTF salts with the transition temperature higher than 10 K, κ-(BEDT-TTF)$_2$Cu(NCS)$_2$, κ-(BEDT-TTF)$_2$Cu[N(CN)$_2$]Br, κ-(BEDT-TTF)$_2$Cu[N(CN)$_2$]Cl and κ-(BEDT-TTF)$_2$CuCN[N(CN)$_2$], have similar layered crystal structure called 'κ-type' The crystal lattice parameters at room temperature are indicated in Table 1.1. The BEDT-TTF molecules are dimerized in pairs and form the conducting layer by the orthogonal arrangement of dimers as shown in Fig. 1.3. This layer serves as a nearly isotropic 2D conducting plane. The counter anion forms polymeric anion chain and constructs insulating plane as shown in Fig. 1.4(a), 1.4(b) and 1.4(c) for κ-(BEDT-TTF)$_2$Cu(NCS)$_2$, κ-(BEDT-TTF)$_2$Cu[N(CN)$_2$]Br and κ-(BEDT-TTF)$_2$CuCN[N(CN)$_2$], respectively [7,16,17]. As a result the crystal is formed by the alternate stacking of the conducting and the insulating planes. Owing to this structure, the electrical conduction is highly 2D. The ratio of the resistivities between the interplane and intraplane directions is $\sim$200 for κ-(BEDT-TTF)$_2$Cu[N(CN)$_2$]Br, $\sim$300 for κ-(BEDT-TTF)$_2$CuCN[N(CN)$_2$], and $\sim$600

6
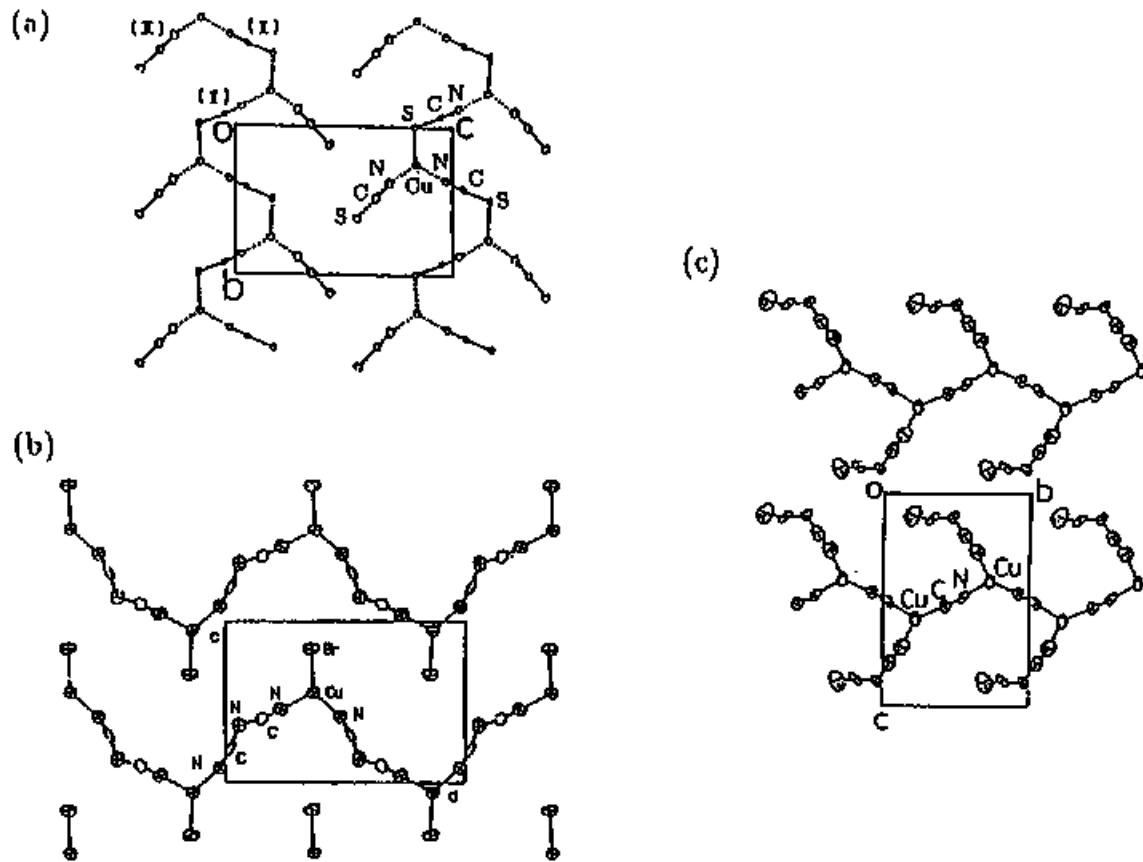
Figure 1.4: The arrangements of the polymeric anion chain of κ-(BEDT-TTF)$_2$Cu(NCS)$_2$ (a), κ-(BEDT-TTF)$_2$Cu[N(CN)$_2$]Br (κ-(BEDT-TTF)$_2$Cu[N(CN)$_2$]Cl) (b) and κ-(BEDT-TTF)$_2$CuCN[N(CN)$_2$] (c), observed from the direction orthogonal to the 2D layer.

for κ-(BEDT-TTF)$_2$Cu(NCS)$_2$. We remark that the Cu atom is monovalent and the d electrons of Cu do not contribute to the conduction, in contrast to the Cu-contained organic conductor DCNQI salts [18–20]

Since the ratio between BEDT-TTF molecules and the counter anion is 2:1, one positive hole per each dimer contributes to the conduction. As a result, the carrier concentration is much lower than the ordinary metals. The tight-binding approximation is a good treatment for the conduction band calculation of the present materials [21]. By applying this approximation and using the highest-occupied-molecular-orbital (HOMO) deduced by the extended Hückel approximation, the Fermi surfaces of κ-(BEDT-TTF)$_2$Cu(NCS)$_2$ and κ-(BEDT-TTF)$_2$Cu[N(CN)$_2$]Br are calculated as shown in Figs. 1.5(a) and 1.5(b), respectively. In the calculation, only the transfer integrals within the conducting plane are considered. The Fermi surface, being reduced within the first Brilliouin zone, consists of two parts, i.e., a warped planer (one-dimensional)

7

Table 1.1: Crystal lattice parameters for κ-type BEDT-TTF salts. For the two salts κ-(BEDT-TTF)$_2$Cu(NCS)$_2$ and κ-(BEDT-TTF)$_2$CuCN[N(CN)$_2$], which belong to monoclinic space group, the interplane direction is along a^* axis, while in κ-(BEDT-TTF)$_2$Cu[N(CN)$_2$]Br and κ-(BEDT-TTF)$_2$Cu[N(CN)$_2$]Cl, which belong to orthorhombic space group, the interplane direction is along b axis. In the former cases, the spacing between BEDT-TTF conducting layers is $a\sin\beta$. In the latter cases, an unit cell extend to two BEDT-TTF layers, so that the spacing between BEDT-TTF conducting layers is $b/2$.

	κ-(BEDT-TTF)$_2$ Cu(NCS)$_2$	κ-(BEDT-TTF)$_2$ CuCN[N(CN)$_2$]	κ-(BEDT-TTF)$_2$ Cu[N(CN)$_2$]Br	κ-(BEDT-TTF)$_2$ Cu[N(CN)$_2$]Cl
	monoclinic	monoclinic	orthorhombic	orthorhombic
a	16.248 Å	16.00 Å	12.942 Å	12.977 Å
b	8.440 Å	8.631 Å	30.016 Å	29.979 Å
c	13.124 Å	12.90 Å	8.539 Å	8.480 Å
β	110.30°	110.97°		
ref.	[16]	[17]	[7]	[8]

electron-like part and a cylindrical (two-dimensional) hole-like part. The crystal structure of κ-(BEDT-TTF)$_2$Cu(NCS)$_2$ and κ-(BEDT-TTF)$_2$CuCN[N(CN)$_2$] belong to the monoclinic space group and there appears a small gap between two parts of the Fermi surface. On the other hand, κ-(BEDT-TTF)$_2$Cu[N(CN)$_2$]Br and κ-(BEDT-TTF)$_2$Cu[N(CN)$_2$]Cl belong to the orthorhombic space group and there is no gap between them. These calculated Fermi surfaces are supported by various magneto-oscillatory phenomena, such as the Shubnikov-de Haas or the de Haas-van Alfen effect [22], and the angular-dependent magnetoresistance oscillation (ADMRO) in the case of κ-(BEDT-TTF)$_2$Cu(NCS)$_2$ [23].

1.3 Purpose and Scope of This Thesis

This thesis deals with the superconductivity transition of κ-type BEDT-TTF organic superconductors possessing the high transition temperature around 10 K under applied magnetic field, paying attention to treat it on the physical basis. Some problems have been pointed out in the treatment of the characteristics of the superconductivity for the organic material. One of them is the broadness of the transition, which is remarkably enhanced by the presence of a magnetic field. As a principal cause of this behavior, the presence of inhomogeneous internal strains has been remarked. However, even in the case of κ-(BEDT-TTF)$_2$Cu[N(CN)$_2$]Br exhibiting a sharp
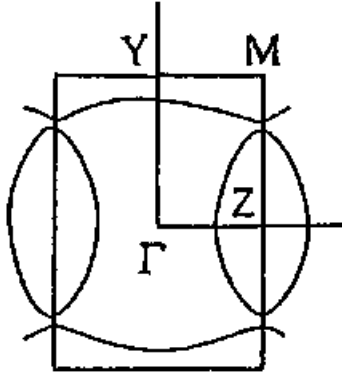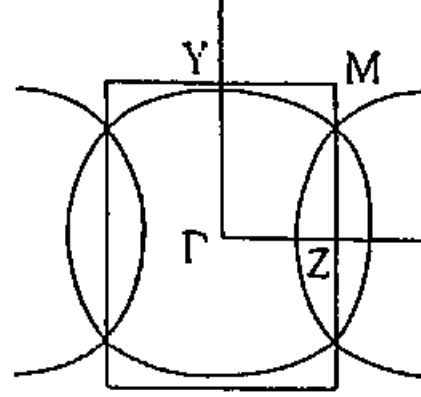
Figure 1.5: The Fermi surface of κ-(BEDT-TTF)$_2$Cu(NCS)$_2$ (a), κ-(BEDT-TTF)$_2$Cu[N(CN)$_2$]Br (b) calculated by the tight-binding approximation of highest-occupied-molecular-orbitals (HOMO).

transition in the absence of magnetic field, considerable broadening by the magnetic field has been observed. This demonstrates clearly that the magnetic field is a principal cause of the broadening. Due to this inherent transition broadening by the magnetic field, the determination of important parameters characterizing the superconductors, such as the upper critical field H_{c2}, and hence the coherence length ξ, becomes often quite misleading if one forces to treat them by the conventional formulae based on the mean-field theory, although it had been useful to characterize the general features in the initial stage of the material development.

In the case of 2D superconductor where the superconductivity coherence length along the inter-plane direction is shorter than the spacing between the planes, the significant anisotropy renders the superconductivity transition quite different from that expected from the mean-field theory. In order to describe the nature of the superconductivity accurately, it is required to treat the two-dimensionality from the starting point. The similar subject has been remarked also for the high-T_c cuprate superconductors. For these cases, vigorous research works covering both experiment and theory have been carried out revealing that the thermal fluctuation effect and the fluxoid dynamics contribute to the broadening in the presence of a magnetic field. We have studied the transition characteristics of the 2D organic superconductors by adopting the theoretical devices. The physical understandings of the superconductivity transition characteristics of κ-type BEDT-TTF superconductors have been promoted by these. Meanwhile we assert that the organic salts

are suitable for the study of the layered superconductor, since they can be prepared as high quality single crystals in contrast to the cuprates. Furthermore, we claim that the size of the required *dc* magnetic field for the study of the mixed state of the BEDT-TTF superconductors is in the laboratory scale. Thus the informations derived through the study with the present superconductors are useful not only to understand the superconducting property of the organic material but also to put forward the investigation of the high-T_c superconductors.

We deal with the effects of the thermal fluctuation and fluxoid dynamics. This thesis consists of six chapters as follows. Following this chapter, the methods of single crystal preparation of the κ-type BEDT-TTF organic superconductors are described in Chapter 2. In Chapter 3, the experimental results and the analysis of *dc* magnetization around the transition region are given. We deal with the result along the renormalized superconductivity fluctuation theory, with which the superconductivity coherence length are evaluated. In Chapter 4, the resistive transition characteristics of κ-type BEDT-TTF salts are discussed in view of the fluctuation effect and the fluxoid pinning, together with the weak-coupling effects notable for κ-(BEDT-TTF)$_2$Cu(NCS)$_2$. In Chapter 5, the frequency and anisotropy of the *ac* susceptibility around the transition region are presented and analyzed along the self-consistent theory of the fluxoid dynamics and the normal (quasiparticle) skin size effects. The fluxoid decoupling effects are also remarked. Summary of this thesis is given in Chapter 6.

Chapter 2

Crystal Growth of κ-Type BEDT-TTF Salt

In this chapter, the methods for the single crystal preparation of the κ-type BEDT-TTF salts are briefly presented. First we describe the method for the growth of κ-(BEDT-TTF)$_2$Cu[N(CN)$_2$]Br crystals used for the measurement in this thesis. Succeedingly, we deal with the cases for κ-(BEDT-TTF)$_2$Cu[N(CN)$_2$]Cl and κ-(BEDT-TTF)$_2$CuCN[N(CN)$_2$], which were grown at Saito's laboratory. Then we refer to the new method developed by Anzai *et al.* This method was applied to the crystal growth of κ-(BEDT-TTF)$_2$Cu(NCS)$_2$ used for resistivity measurements described in Chapter 4.

2.1 κ-(BEDT-TTF)$_2$Cu[N(CN)$_2$]Br

Single crystals of κ-(BEDT-TTF)$_2$Cu[N(CN)$_2$]Br were grown by an electrochemical oxidation method using a glass cell with platinum electrodes shown in Fig. 2.1 [24]. The BEDT-TTF molecules were oxidized under a constant current in the presence of CuBr, NaN(CN)$_2$ and 18-crown-6 ether. As a solvent, THF (tetrahydrofuran) with 10% ethanol was used. To remove contaminant, the reagents were recrystallized and the solvents were distilled. Typical concentrations of the BEDT-TTF and other reagents were 1×10^{-3} mol/l and 1×10^{-2} mol/l, respectively. The current of 0.5 μA was fed. It is considered that the reaction proceeds as follows. First, 18-crown-6 ether extracts Na$^+$ from NaN(CN)$_2$. CuBr and N(CN)$_2^-$ combine together to compose Cu[N(CN)^2]Br$^-$ and crystallize with BEDT-TTF on the anode, where excess negative charges are absorbed. The reagents and solvent are mixed together under a dry nitrogen atmosphere. During the crystal growth, the growth cell was kept in dark. It took about two weeks to get single crystals of black rhombic platelets with dimensions of 1~2 mm. After harvest, the crystals were washed with ethanol and dried in vacua. Then we selected a single crystal of well-shaped rhombic shape.

anode   cathod

teflon holder

N$_2$ gas

Pt electrode
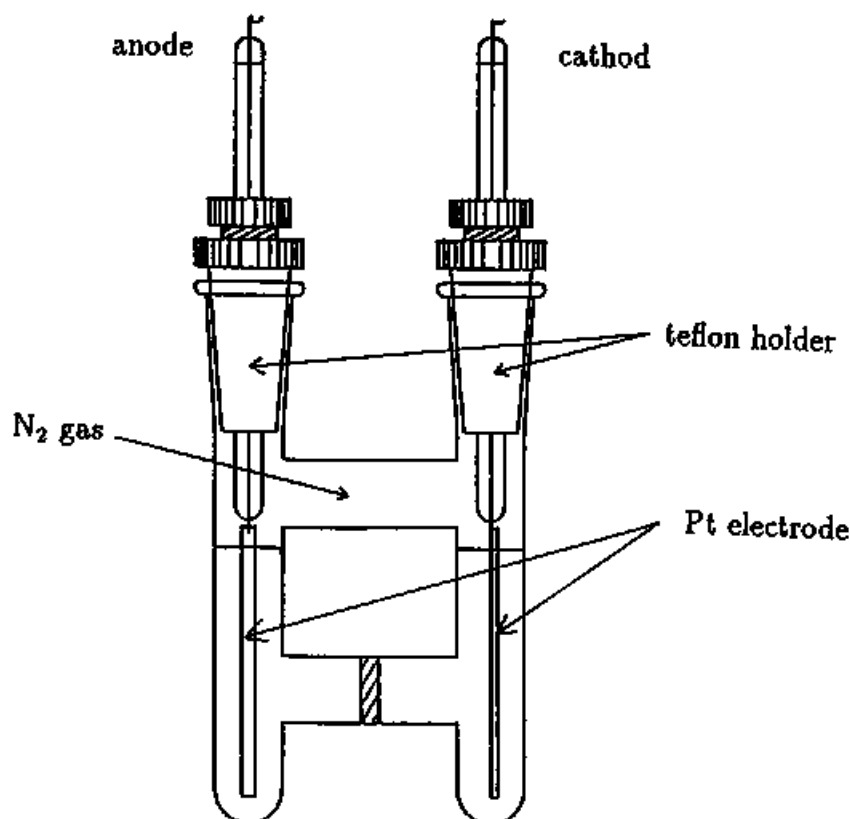
Figure 2.1: The glass cell used to obtain κ-(BEDT-TTF)$_2$Cu[N(CN)$_2$]Br single crystals by electrochemical method.

The sample size of the good shaped crystal is approximately 1mm×1mm×0.2mm.

2.2 κ-(BEDT-TTF)$_2$Cu[N(CN)$_2$]Cl and κ-(BEDT-TTF)$_2$ CuCN-[N(CN)$_2$]

For the titled two salts, crystals with other phase are often yielded as co-products: semiconducting (BEDT-TTF)$_2$CuCl$_2$ for the former salt, and metallic κ'-(BEDT-TTF)$_2$Cu$_2$(CN)$_3$ or semiconducting θ-(BEDT-TTF)$_2$Cu$_2$(CN)[N(CN)$_2$]$_2$ for the latter salt. The efficiency for harvesting the object single crystal is worse than the case for κ-(BEDT-TTF)$_2$Cu[N(CN)$_2$]Br. The present methods by Saito et al. are essentially similar with use of the electrochemical oxidation as the cases of κ-(BEDT-TTF)$_2$Cu[N(CN)$_2$]Br. The reagents are (C$_6$H$_5$)$_4$PN(CN)$_2$ and CuCl for κ-(BEDT-TTF)$_2$Cu[N(CN)$_2$]Cl ; (C$_6$H$_5$)$_4$PN(CN)$_2$ and CuCN for κ-(BEDT-TTF)$_2$CuCN[N(CN)$_2$]. The solvent is Ph-CN (benzonitrile) for both salts with small amount of ethanol. The growth current is ~ 0.2 μA. It takes one month to get crystals, if everything goes well.

12

2.3 Crystal Growth of κ-(BEDT-TTF)$_2$Cu(NCS)$_2$ by Current Regulation Method

Single crystals of κ-(BEDT-TTF)$_2$Cu(NCS)$_2$ can be prepared by the similar electrochemical method. The best reagents are CuSCN, KSCN and 18-crown-6 ether. The solvent is 1,1,2-trichloroethan with 10 % ethanol. Addition of alcohol (methanol is also useful) is found to be an essential condition to get large crystal. Using this conventional method, the crystals used for magnetization measurement were grown.

As will be discussed in Chapter 4, we needed high-quality defect-reduced samples to extract the intrinsic behavior of the resistivity, especially in the case of κ-(BEDT-TTF)$_2$Cu(NCS)$_2$. We adopted the high-quality single crystal grown by Anzai *et al.*, obtained by a current-regulation method [25]. They consider that the current fed during the crystal growth should be increased with the progress of crystal growth. Along this idea, the current (I) density per unit sample surface are kept constant throughout the growing process, i.e., $I/S = constant$, where S is the area of the sample surface. Then the current has to be fed is given as a function of time (t) like $I = ct^2$, where c is a constant. Using this current-regulation method, well-shaped hexagonal single crystals are obtained with typical size of 1mm×1mm×0.2mm. Their surface looks more smooth and shiny compared with the crystals grown by the conventional constant-current method.

Chapter 3

dc Magnetization near Transition

In this chapter, we describe the superconductivity transition under external magnetic field for the κ-type BEDT-TTF salts, such as κ-(BEDT-TTF)$_2$Cu(NCS)$_2$ and κ-(BEDT-TTF)$_2$Cu-[N(CN)$_2$]Br, observed through the dc magnetization measurements around the transition region. The temperature and magnetic field dependences of the magnetization are analyzed in terms of the renormalized superconductivity-fluctuation theory developed for layered superconductors in a magnetic field. We discuss on the superconductivity coherence lengths obtained along the analysis.

3.1 Experimental Procedure

The dc magnetization measurements were carried out under field-cooled condition by a SQUID magnetometer, as a function of temperature (T) around the transition region under external dc magnetic fields (H) from 0.05 to 1 tesla. A single crystal of superconductor was set in a Diflon sample holder, so that its conducting plane was perpendicular to the external dc magnetic field. This configuration enables the analysis after the fluctuation theory described in §3.3. In this chapter we restrict the magnetization in the reversible region above the irreversibility line, where the magnetization does not depend on the thermal history. We will mention the problem of irreversibility later in Chapter 5.

In order to deduce the diamagnetic component related to the superconductivity transition, we subtract the smoothly extrapolated magnetization observed in the higher temperature region so that the magnetization around 16 K is set to be zero. In the experiment the single crystals of κ-(BEDT-TTF)$_2$Cu(NCS)$_2$ and κ-(BEDT-TTF)$_2$Cu[N(CN)$_2$]Br are used.

We evaluate the effect of isotopic substitution of BEDT-TTF molecule on the transition characteristics through the measurements on the salts synthesized using BEDT-TTF molecules with

14

deuterated or ^{13}C-substituted terminal ethylene bases.

We concentrate on two kinds of salts, κ-(BEDT-TTF)$_2$Cu(NCS)$_2$ and κ-(BEDT-TTF)$_2$Cu-[N(CN)$_2$]Br in this chapter. The single crystal of κ-(BEDT-TTF)$_2$CuCN[N(CN)$_2$] is too small and thin to get enough signal for the analysis. We also exclude the case for κ-(BEDT-TTF)$_2$Cu-[N(CN)$_2$]Cl, which does not show superconductivity at ambient pressure.

3.2 Magnetic Transition Characteristics

We show the temperature and dc magnetic field dependence of dc magnetization of κ-(BEDT-TTF)$_2$Cu(NCS)$_2$ and κ-(BEDT-TTF)$_2$Cu[N(CN)$_2$]Br in Fig. 3.1 and Fig. 3.2, respectively. The external magnetic field is applied perpendicular to the 2D plane. The data are in the reversible region above the irreversibility line. In this region, fluxoids in the mixed state do not affect the static thermodynamic quantity. Due to the rounding of the magnetization transition in the critical region and the broadness of the growth of diamagnetic signal under magnetic field, it is hard to determine the transition point by the method applied to the classical superconductors, and hence the upper critical field, directly from these data. In the following, we apply the superconductivity fluctuation analysis to explain the specific behaviors and deduce the important parameters characterizing the superconductivity state, such as ξ and H_{c2}.

3.3 Outline of the Renormalized Fluctuation Theory

Prior to the analysis, we summarize the theoretical treatment of the superconductivity fluctuation. The fluctuation conductivity above T_c in the layered superconductor has been treated by Lawrence and Doniach through modeling it as a set of 2D superconductors interacting via Josephson mechanism [26]. They formulated the Ginzburg Landau free energy as,

$$F = \sum_i \left[\alpha |\psi_i|^2 + \frac{\beta}{2} |\psi_i|^4 + \frac{1}{2m^*} \left| (-i\hbar\nabla - \frac{2eA}{c})\psi_i \right|^2 + \eta |\psi_{i+1} - \psi_i|^2 \right] + \frac{B^2}{8\pi} , \qquad (3.1)$$

where the index i runs over the 2D superconducting layers. First three terms represent the 2D superconductivity of each layer. m^* is the effective mass and α is written as,

$$\alpha = \frac{\hbar^2}{4m^*\xi_{\|}^2}\epsilon ,$$

15

Figure 3.1: The temperature dependence of the *dc* magnetization of κ-(BEDT-TTF)$_2$Cu(NCS)$_2$ in the reversible region under magnetic field perpendicular to the 2D plane. (Solid lines are guide for eyes.)
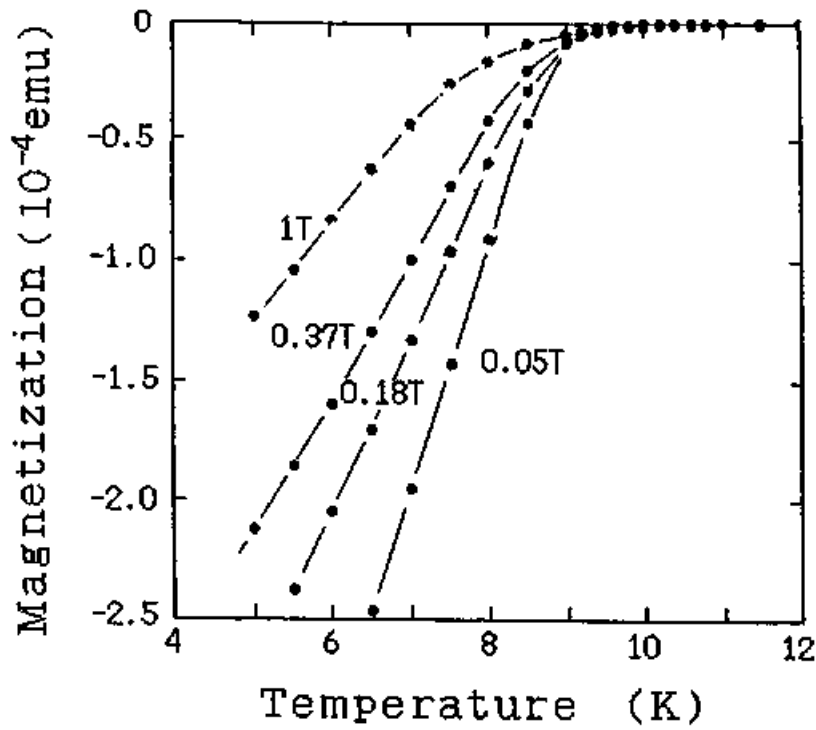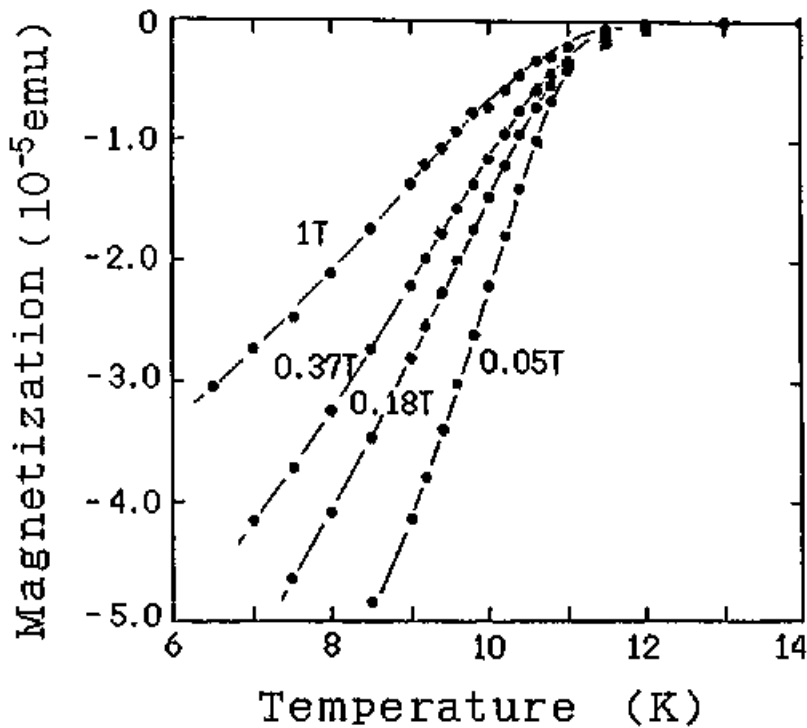

Figure 3.2: The temperature dependence of the *dc* magnetization of κ-(BEDT-TTF)$_2$Cu[N(CN)$_2$]Br in the reversible region under magnetic field perpendicular to the 2D plane. (Solid lines are guide for eyes.)

16

where $\xi_\parallel$ is a superconductivity coherence length of each 2D layer, i.e., the intraplane coherence length at absolute zero temperature. (Hereafter we denote $\xi_\parallel$ and $\xi_\perp$ for the intraplane and interplane superconductivity coherence length *at absolute zero temperature*.) ϵ is a reduced temperature defined as $\epsilon = (T - T_{c0})/T_{c0}$, where T_{c0} is the superconductivity transition temperature at zero magnetic field. In thier calculation the third term $\beta/2|\psi_i|^4$ is neglected, since they treat the temperature region above T_c, where amplitude of order parameter ψ is small enough. (This term becomes important later to treat the phenomena below T_c.) The fourth term $\eta|\psi_{i+1} - \psi_i|^2$ represent the interaction between the superconducting layers, formulated as Josephson coupling between i-th and $i+1$-th layers.

By taking the variation of (3.1) with respect to the vector potential A, we obtain the in-plane supercurrent. Substituting it into Kubo formula, we obtain the intraplane conductivity due to the supercurrent contribution as,

$$\sigma = \frac{e^2}{16\hbar d}\frac{1}{\epsilon\sqrt{1+\lambda}} \tag{3.2}$$

The parameter $\lambda = (2\xi_\perp/d)^2$ scales the strength of two-dimensionality. $\xi_\perp$ is the superconductivity coherence length in the interplane direction and d is the interplane spacing. This formula has been extended by Hikami and Larkin to include the effect of magnetic field as [27],

$$\sigma = \int_0^{2\pi/d} \frac{e^2}{8\hbar\epsilon_k}\left(\frac{\epsilon_k}{h}\right)^2\left[\psi(\frac{1}{2} + \frac{\epsilon_k}{2h}) - \psi(1 + \frac{\epsilon_k}{2h}) + \frac{h}{\epsilon_k}\right]\frac{dk}{2\pi} , \tag{3.3}$$

where $\epsilon_k = \epsilon(1 + \lambda/2(1 - \cos kd))$ and h is a reduced magnetic field defined as,

$$h = \frac{B}{H_{c2}(0)} = \frac{2\pi\xi_\parallel^2}{\phi_0}B, \tag{3.4}$$

and $\psi(x)$ is a di-Gamma function.

These theoretical treatments adopt Gaussian approximation, in which the $|\psi|^4$ term in the Ginzburg Landau functional is neglected. This treatment is valid above T_c, where the long-time average of the order parameter ψ is zero. These formulae succeeded in explaining the observed excess fluctuation conductivity above T_c; often observed as a rounding of the resistivity just above T_c. However, below T_c where order parameter ψ grows large with nonvanishing time average, the $|\psi|^4$ term cannot be neglected.

To develop the formulae applicable below T_c and explain the transition characteristics under a magnetic field, we must take account of the $|\psi|^4$ term. Ikeda *et al.* have renormalized the mass parameters of *Landau levels* taking account of the $|\psi|^4$ term [28–30]. The Ginzburg-Landau equation characterizing the order parameter ψ becomes the same form as the Schlödinger equation of a charged particle in a magnetic field, if we lay aside the $|\psi|^4$ term. As is well-known, a charged particle under magnetic field draws the Landau orbit, whose energy spectrum is represented by the Landau levels. Along this theoretical analogy, the conductivity given in (3.3) can be rewritten as the summation over the hypothetical Landau levels [28],

$$\rho_{xx} = \frac{e^2}{2\hbar\xi_\perp}\hbar^2 \sum_{n=0}^\infty \frac{n+1}{(\mu_{n+1R}-\mu_{nR})^2}(f_n + f_{n+1} - 2f_{n+1/2}) , \qquad (3.5)$$

where

$$f_n = \frac{1}{\sqrt{\mu_{nR}(1+\lambda^{-1}\mu_{nR})}} ,$$

$$f_{n+1/2} = \frac{1}{\sqrt{\tilde{\mu}_{nR}(1+\lambda^{-1}\tilde{\mu}_{nR})}} ,$$

$$\tilde{\mu}_{nR} = (\mu_{nR} + \mu_{n+1R})/2$$

In the Gaussian approximation, the mass of each Landau level is written as,

$$\mu_{nR} = \mu_0 + 2nh = \epsilon + h + 2nh$$

In this formulation, we can take account of the effect of the $|\psi|^4$ term by renormalizing the mass parameters μ_{nR}. The renormalized mass parameters are calculated by solving the self-consistent equation below, written implicitly using a parameter of,

$$\beta_0 = 1 + \frac{2}{\lambda}\mu_{0R} \qquad (3.6)$$

For $n = 0$ (the lowest Landau level), the equation becomes as,

$$\mu_{0R} = \mu_0 + \frac{g_3}{\sqrt{\lambda(\beta_0^2-1)}} + \frac{\lambda\sqrt{\beta_0^2-1)}}{8\beta_0}\left[\ln\frac{\gamma_+}{\alpha_+} + \frac{\alpha-\beta_0}{\sqrt{\beta_0^2-1}}\ln\left(\frac{\beta_0\gamma+\sqrt{(\beta_0^2-1)(\gamma^2-1)}-1}{\beta_0\alpha+\sqrt{(\beta_0^2-1)(\alpha^2-1)}-1}\right)\right] ,$$
$$(3.7)$$

where

$$\alpha = 2\beta_0^2 - 1 \, ,$$

$$\gamma = \alpha + \frac{8g_3\beta_0}{\sqrt{\lambda^3(\beta_0^2 - 1)}} \, ,$$

$$\alpha_+ = \alpha + \sqrt{\alpha^2 - 1} \, ,$$

$$\gamma_+ = \gamma + \sqrt{\gamma^2 - 1}$$

Here, the parameter g_3 is related to the gap of specific heat at the superconductivity transition ΔC as,

$$g_3 = \frac{k_B}{\Delta C} \frac{B}{\phi_0 \xi_\perp} \tag{3.8}$$

For $n \geq 1$, the equation to be solved is,

$$
\begin{aligned}
\mu_{nR} &= \mu_0 + 2nh + \frac{g_3}{\sqrt{\lambda(\beta_0^2 - 1)}} + \frac{\lambda\sqrt{\beta_0^2 - 1)}}{8\beta_0(n+1)!} \\
&\quad \times \left\{ \left(\ln \frac{\gamma_+}{\alpha_+} \right)^{n+1} + \frac{\alpha - \beta_0}{\sqrt{\beta_0^2 - 1}} \left[\ln \left(\frac{\beta_0\gamma + \sqrt{(\beta_0^2 - 1)(\gamma^2 - 1)} - 1}{\beta_0\alpha + \sqrt{(\beta_0^2 - 1)(\alpha^2 - 1)} - 1} \right) \right]^{n+1} \right\}
\end{aligned}
\tag{3.9}
$$

Since the detailed knowledge of μ_{nR} for $n \geq 2$ is not significant numerically on the evaluation of the involved physical quantities, we use simplified expressions for $n \geq 2$ as,

$$\mu_{nR} = \mu_{0R} + 2nh \tag{3.10}$$

By using (3.5~10), we can calculate the intraplane conductivity as a function of temperature and applied magnetic field, with parameters such as the transition temperature at zero magnetic field (T_{c0}), the intraplane and the interplane superconductivity coherence lengths ($\xi_\parallel$ and $\xi_\perp$) (at the absolute zero temperature) and the gap of specific heat at the superconductivity transition (ΔC).

For the conductivity in the interplane direction, we use the following formula,

19

$$\rho_{xx} = \frac{e^2}{32\hbar\xi_\perp}\left(\frac{\xi_\perp}{\xi_\parallel}\right)^2 h\sum_{n=0} f_n^3 \qquad (3.11)$$

For the magnetization, the temperature derivative of magnetization is calculated from the temperature and magnetic field derivatives of Ginzburg-Landau free energy F per unit volume.

$$\frac{\partial M}{\partial T} = -\frac{\partial}{\partial B}\frac{\partial}{\partial T}F \qquad (3.12)$$

The results is formulated as,

$$
\begin{aligned}
\frac{\partial M}{\partial T} &= \frac{k_B\sqrt{\lambda}}{2\phi_0\xi_\perp}\Big\{\, E_0(-1 + h\frac{\partial\mu_{0R}}{\partial h}(\mu_{0R} + \frac{\lambda}{2})E_0^2) \\
&\quad +2E_2(1 + 2h(\mu_{0R} + 4h + \frac{\lambda}{2})E_2^2) \\
&\quad -E_1(1 - h\frac{\partial\mu_{1R}}{\partial h}(\mu_{1R} + \frac{\lambda}{2})E_1^2) + \sum_{n=2}(n+1) \\
&\quad \times(-E_n + E_{n+1} + 2h(\mu_{0R} + 2(n+1)h + \frac{\lambda}{2})E_{n+1}^3) \\
&\quad +h\frac{\partial\mu_{0R}}{\partial h}\sum_{n=2}(\mu_{0R} + 2nh + \frac{\lambda}{2})E_n^3 \,\Big\},
\end{aligned} \qquad (3.13)
$$

where

$$E_n = \frac{1}{\sqrt{\mu_{nR}(\mu_{nR} + \lambda)}}$$

The forms for the various partial derivatives appearing in (3.13) are given explicitly in [30].

3.4 Analysis : Deduction of Coherence Length

By numerically integrating (3.13) with respect to the temperature as,

$$M = \int_T^{T_0}\frac{\partial M}{\partial T}dT, \qquad (3.14)$$

the temperature and magnetic field dependences of the magnetization are calculated in the renormalized fluctuation regime. In the following we search appropriate parameters as transition temperature (T_{c0}) and interplane ($\xi_\perp$) and intraplane ($\xi_\parallel$) coherence length to reproduce the experimental data given in Fig. 3.1 and Fig. 3.2. Here we set the upper limit T_0 of the integral (3.14) as 16 K, where we assume that the superconductivity contribution of the magnetization is zero.

20

The gap of the specific heat at the superconductivity transition (ΔC) is given by several authors. The values for κ-(BEDT-TTF)$_2$Cu(NCS)$_2$ are 7.3×10^2 mJ/K·mol by Andraka *et al.* [31], and 5.3×10^2 mJ/K·mol by Graebner *et al.* [32]. For κ-(BEDT-TTF)$_2$Cu[N(CN)$_2$]Br, the value of 5.2×10^2 mJ/K·mol is given by Andraka *et al.* [33]. For the present analysis we employ the values of 6.0×10^2 mJ/K·mol for κ-(BEDT-TTF)$_2$Cu(NCS)$_2$ and 5.2×10^2 mJ/K·mol for κ-(BEDT-TTF)$_2$Cu[N(CN)$_2$]Br. We confirm that the variation of ΔC by 10 % around the values does not change the derived value of ξ by more than 10 %. Finally we set the interplane spacing d to be 1.52 nm for κ-(BEDT-TTF)$_2$Cu(NCS)$_2$ and 1.48 nm for κ-(BEDT-TTF)$_2$Cu[N(CN)$_2$]Br from the low-temperature X-Ray crystallographic data [34].

Proper fittings of the calculated to the experimental data lead the values of the interplane $\xi_\perp$ and intraplane $\xi_\parallel$ to be $\xi_\perp = 0.31 \pm 0.05$ nm and $\xi_\parallel = 2.9 \pm 0.5$ nm with $T_{c0} = 8.7 \pm 0.2$ K for κ-(BEDT-TTF)$_2$Cu(NCS)$_2$. As mentioned formerly, these values are the coherence length at the absolute zero temperature. The uncertainty is relevant to the evaluation of the fitness of the calculated lines, but includes the uncertainties due to ΔC. We notice that the derived value of T_{c0} is smaller than the value of 10.4 K derived from the midpoint of the resistive transition. As will be discussed in Chapter 4, the values of T_c obtained from resistivity measurements are sometimes misleading, due to the current path problem. Furthermore, at zero magnetic field, Kosterlitz-Thouless-like transition characteristic for highly 2D superconductor may alter the resistive transition characteristics considerably. We assert that the value $T_c = 8.7 \pm 0.2$ K should be adopted as the bulk superconductivity transition temperature of κ-(BEDT-TTF)$_2$Cu(NCS)$_2$. Thermodynamic measurements, such as specific heat, often deduce T_c close to this value [32]. For κ-(BEDT-TTF)$_2$Cu[N(CN)$_2$]Br, the values $\xi_\perp = 0.58 \pm 0.1$ nm, $\xi_\parallel = 2.3 \pm 0.4$ nm with $T_{c0} = 10.9 \pm 0.2$ K are obtained. In this case the discrepancy in T_c between the previous estimation as 11.6 K is smaller than in the case of κ-(BEDT-TTF)$_2$Cu(NCS)$_2$. The fitted magnetization curves are shown in Fig. 3.3 and Fig. 3.4 for κ-(BEDT-TTF)$_2$Cu(NCS)$_2$ and κ-(BEDT-TTF)$_2$Cu[N(CN)$_2$]Br, respectively.

We notice that the values for κ-(BEDT-TTF)$_2$Cu[N(CN)$_2$]Br are rather close to the values, $\xi_\perp = 0.4$ nm and $\xi_\parallel = 3.7$ nm, by Kwok *et al.* [35], as shown in Table 3.1, which was derived by the application of the ordinary mean field theory useful to three-dimensional system to the magnetization data. In the mean time, the present values for κ-(BEDT-TTF)$_2$Cu(NCS)$_2$ are much shorter than the reported values of $\xi_\perp = 0.96$ nm and $\xi_\parallel = 18.2$ nm, estimated from the resistive
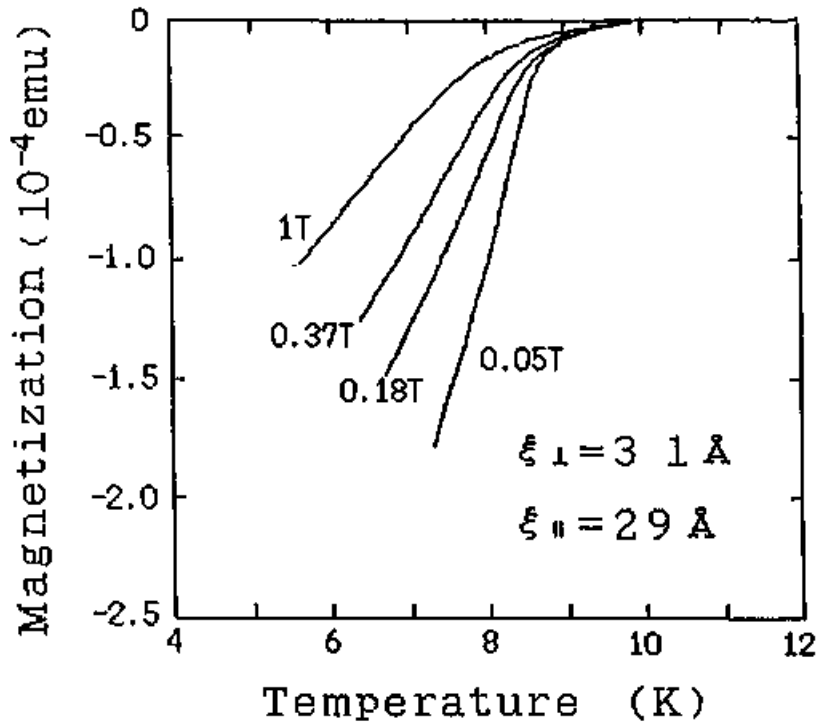
Figure 3.3: The calculated *dc* magnetization of κ-(BEDT-TTF)$_2$Cu(NCS)$_2$ using (3.14). The parameters used are $\xi_\perp = 0.31$ nm, $\xi_\parallel = 2.9$ nm, and $T_{c0} = 8.7$ K.
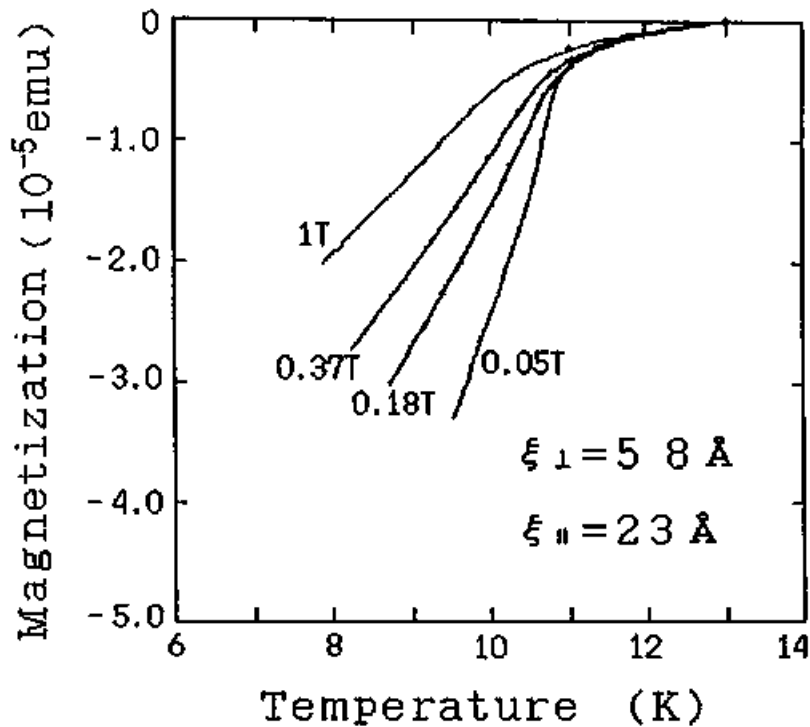

Figure 3.4: The calculated *dc* magnetization of κ-(BEDT-TTF)$_2$Cu[N(CN)$_2$]Br using (3.14). The parameters used are $\xi_\perp = 0.58$ nm, $\xi_\parallel = 2.3$ nm, and $T_{c0} = 10.8$ K.

Table 3.1: The superconductivity coherence lengths for κ-(BEDT-TTF)$_2$Cu(NCS)$_2$ and κ-(BEDT-TTF)$_2$Cu[N(CN)$_2$]Br derived from the analysis of dc magnetization with respect to the renormalized fluctuation theory. The results for the salts with isotope-substituted BEDT-TTF molecules are also shown. H-salt, D-salt and ^{13}C-salt denote the salts synthesized with hydrogenated or deuterated or ^{13}C-substituted BEDT-TTF molecules, respectively.

	T_{c0} (K)	$\xi_\perp$ (nm)	$\xi_\parallel$ (nm)
κ-(BEDT-TTF)$_2$Cu(NCS)$_2$ (d=1.52 nm)			
H-salt	8.7±0.2	0.31±0.05	2.9±0.5
D-salt	9.0±0.2	0.32±0.05	2.9±0.5
^{13}C-salt	8.6±0.2	0.31±0.05	2.9±0.5
Graebner *et al.*[32]	9.4	0.3	6.5
Oshima *et al.*[36]	10.4	0.96	18.2
Murata *et al.*[37]	10.5	0.77	14.3*
κ-(BEDT-TTF)$_2$Cu[N(CN)$_2$]Br (d=1.48 nm)			
H-salt	10.9±0.2	0.58±0.1	2.3±0.4
D-salt	10.6±0.2	0.57±0.1	2.3±0.4
^{13}C-salt	10.9±0.2	0.58±0.1	2.3±0.4
Kwok *et al.*[35]	10.8±0.05	0.4	3.7

* The value is given by $\sqrt{\xi_b \xi_c}$, where ξ_b=17.4 nm, ξ_c=11.8 nm

transition measurements [36,37]. Here we should remind that for organic superconductors, ξ had been derived in most cases from the broad resistive transition under a magnetic field by assuming that the transition temperature $T_c(H)$ exists at either onset or midpoint of the broad transition. The criterion had changed from material to material or case by case, since there were no useful theoretical devices as adopted here to treat with the problem.

The discrepancy between the deduced value by the fluctuation analysis here and the previous estimation is more severe for κ-(BEDT-TTF)$_2$Cu(NCS)$_2$ than for κ-(BEDT-TTF)$_2$Cu[N(CN)$_2$]Br. This fact indicates that κ-(BEDT-TTF)$_2$Cu[N(CN)$_2$]Br is closer to the conventional superconductor than κ-(BEDT-TTF)$_2$Cu(NCS)$_2$, i.e., κ-(BEDT-TTF)$_2$Cu[N(CN)$_2$]Br is less 2D than κ-(BEDT-TTF)$_2$Cu(NCS)$_2$. This is also indicated by the difference in the interplane coherence length in comparison with the interplane spacing of $\sim$ 1.5 nm. This point will be mentioned again in the next section in relation to the scaling analysis.
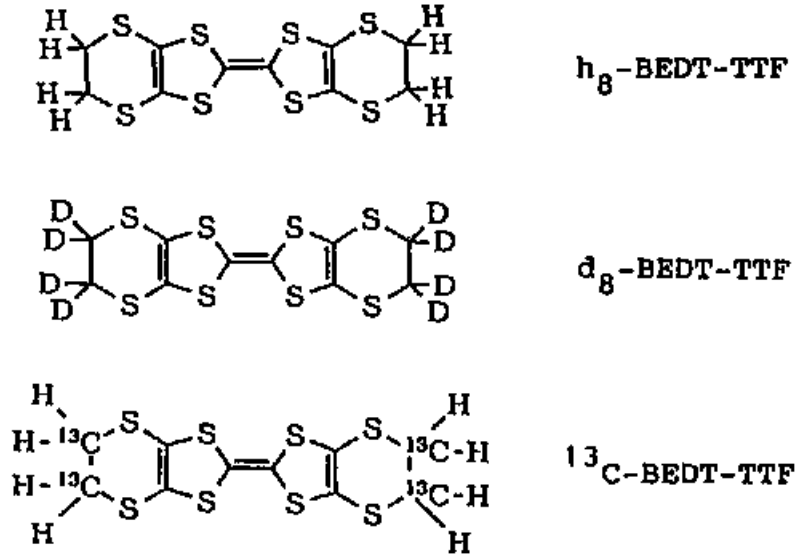
Figure 3.5: The isotope-substituted BEDT-TTF molecules.

3.5 Discussion

In this section, we first examine the effect of isotope substitution of the terminal ethylene base of BEDT-TTF molecule on the superconductivity coherence length. Next we throw attention to the scaling property of the fluctuation at two- or three-dimension. This treatment is useful to evaluate the probable upper critical field H_{c2} in the presence of fluctuation effect.

3.5.1 Effect of isotope substitution

The effects of the isotope substitution of the BEDT-TTF molecules on the superconductivity transition characteristics have been remarked for the BEDT-TTF superconductors, due to the large isotope shift in T_c in comparison with the conventional superconductors. To evaluate the effects of isotope substitution on the superconductivity coherence length, dc magnetization measurements have been carried out for κ-(BEDT-TTF)$_2$Cu(NCS)$_2$ synthesized using BEDT-TTF molecules possessing deuterated or ^{13}C-substituted terminal ethylene bases (d$_8$-BEDT-TTF and ^{13}C-BEDT-TTF, shown in Fig. 3.5). The results are shown in Fig. 3.6(a) for κ-(BEDT-TTF)$_2$Cu(NCS)$_2$, where we normalized the magnetization M so that the similarity of the data with those for h$_8$-BEDT-TTF salts is demonstrated with the function of the reduced temperature $\epsilon = (T - T_{c0})/T_{c0}$. Further, the results for κ-(BEDT-TTF)$_2$Cu[N(CN)$_2$]Br with d$_8$-BEDT-TTF
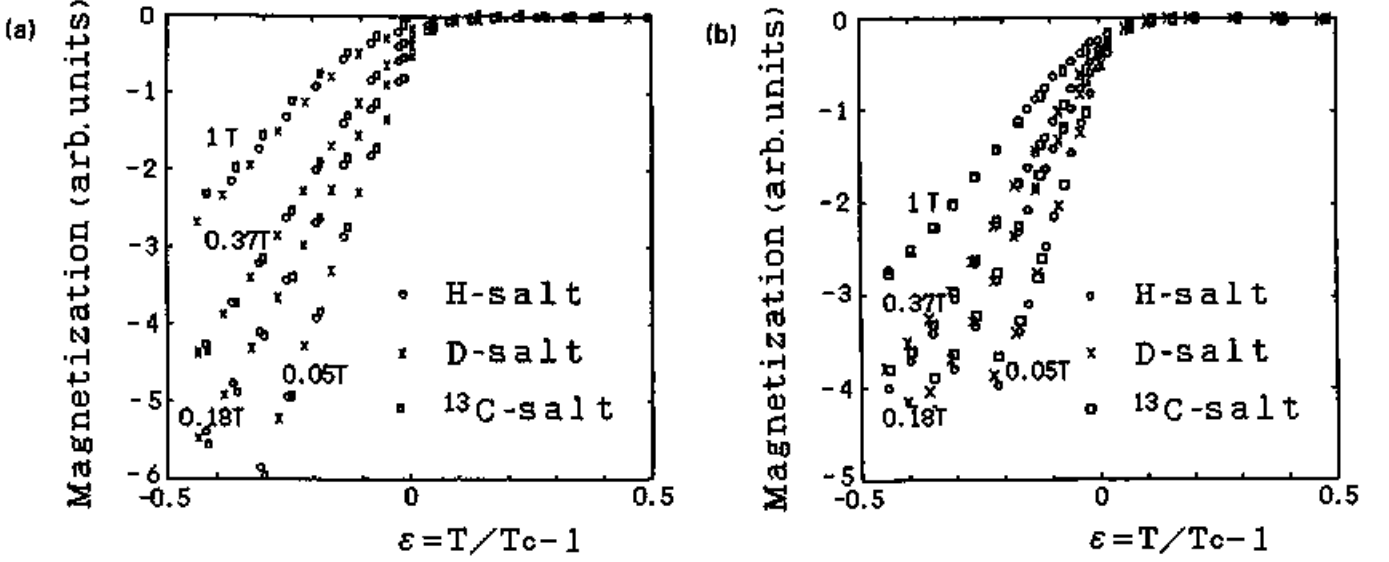
24

Figure 3.6: Comparison of the measured dc magnetization of salts with isotope-substituted BEDT-TTF for κ-(BEDT-TTF)$_2$Cu(NCS)$_2$ (a) and for κ-(BEDT-TTF)$_2$Cu[N(CN)$_2$]Br (b). The horizontal axis is scaled with the reduced temperature $\epsilon = (T - T_{c0})/T_{c0}$. Magnitudes of the diamagnetic signals are equalized by multiplying constant factors. H-salt, D-salt and ^{13}C-salt denote the salts synthesized with BEDT-TTF possessing hydrogenated, deuterated and ^{13}C-substituted terminal ethylene bases, respectively.

and with ^{13}C-BEDT-TTF are shown together with h$_8$-BEDT-TTF case in Fig. 3.6(b). The values of $\xi_\perp$ and $\xi_\parallel$ derived as appropriate fitting parameters for these measured results are listed in Table 3.1.

Here we have to remark the value of ΔC for d$_8$-BEDT-TTF and ^{13}C-BEDT-TTF salts used for the analysis. It is found that the isotope substitution shifts in T_c are rather consistent with previous reports [38,39], but we have no data of ΔC for salts with d$_8$-BEDT-TTF and ^{13}C-BEDT-TTF molecules. Then, by taking account of the relations, $\xi = a\hbar v_F/k_B T_c$ and $\Delta C/\gamma T_c = b(=1.43)$ applicable to BCS superconductors, where a is a constant of the order of one, v_F is the Fermi velocity and γ is the Sommerfeld constant, ΔC for the isotope-substituted salt is evaluated by taking b as a constant. We find that $\xi_\perp$ changes with T_{c0}, as shown in Table 3.1., whereas $\xi_\parallel$ is insensitive to the substitution.

The similarity of the temperature dependences of the magnetization, as shown in Figs. 3.6(a) and 3.6(b), is surprising, if we take account of the temperature dependences of the normal resistance of κ-(BEDT-TTF)$_2$Cu[N(CN)$_2$]Br. The normal resistivity behavior is quite different for

hydrogenated and deuterated salt of κ-(BEDT-TTF)$_2$Cu[N(CN)$_2$]Br [24].

3.5.2 Scaling treatment of fluctuation

The broad diamagnetic superconductivity transition under magnetic field by the thermal fluctuation obscures the transition (nucleation) point under magnetic field $T_c(H)$. In order to evaluate the value of $T_c(H)$ in the sense of the mean-field treatment in the presence of fluctuation effects, we perform the scaling analysis of the observed magnetization in which the temperature and magnetic field dependences of the magnetization are scaled by a variable [40,41],

$$t_G = \frac{T - T_c(H)}{(TH)^n} , \tag{3.15}$$

$$n = \begin{cases} 2/3 & \text{for 3D case} \\ 1/2 & \text{for 2D case.} \end{cases}$$

This scaling property can be also deduced from (3.13) in the two- or three-dimensional limit [42].

By choosing the values for $T_c(H)$ to get a universal scale fit, we get plots shown in Figs. 3.7(a) and 3.7(b) for κ-(h$_8$-BEDT-TTF)$_2$Cu(NCS)$_2$ and Figs. 3.8(a) and 3.8(b) for κ-(h$_8$-BEDT-TTF)$_2$Cu[N(CN)$_2$]Br, respectively, where Figs. 3.7(a) and 3.8(a) are for the case for 2D system and Figs. 3.7(b) and 3.8(b) are for 3D one. The derived values of $T_c(H)$ are given in the inset.

For κ-(BEDT-TTF)$_2$Cu(NCS)$_2$, the 2D fit gives a universal relation for magnetic fields, higher than 0.18 T, whereas the 3D fit gives deviation as approaching $T_c(H)$. This suggests that the 2D treatment is more appropriate for κ-(BEDT-TTF)$_2$Cu(NCS)$_2$. On the other hand, the universality for κ-(BEDT-TTF)$_2$Cu[N(CN)$_2$]Br is not so satisfactory as for the κ-(BEDT-TTF)$_2$Cu(NCS)$_2$. This difference in the adequacy for scaling treatment between two salts indicates that κ-(BEDT-TTF)$_2$Cu(NCS)$_2$ is more 2D than κ-(BEDT-TTF)$_2$Cu[N(CN)$_2$]Br. κ-(BEDT-TTF)$_2$Cu[N(CN)$_2$]Br is not so 2D, but it is still far from 3D cases. Thus an appropriate treatment of κ-(BEDT-TTF)$_2$Cu[N(CN)$_2$]Br lies in the intermediate of 2D and 3D.

The obtained $T_c(H)$ is plotted against the magnetic field in Fig. 3.9 for both 2D and 3D treatments. This figure may be read as the upper critical field $H_{c2}(T)$ versus temperature T relation. In the figure, $H_{c2}(T)$ versus T relation for κ-(BEDT-TTF)$_2$Cu(NCS)$_2$ reported by Oshima *et al.*, [36] is reproduced as a reference. The scaling analysis of the magnetization is recently carried out
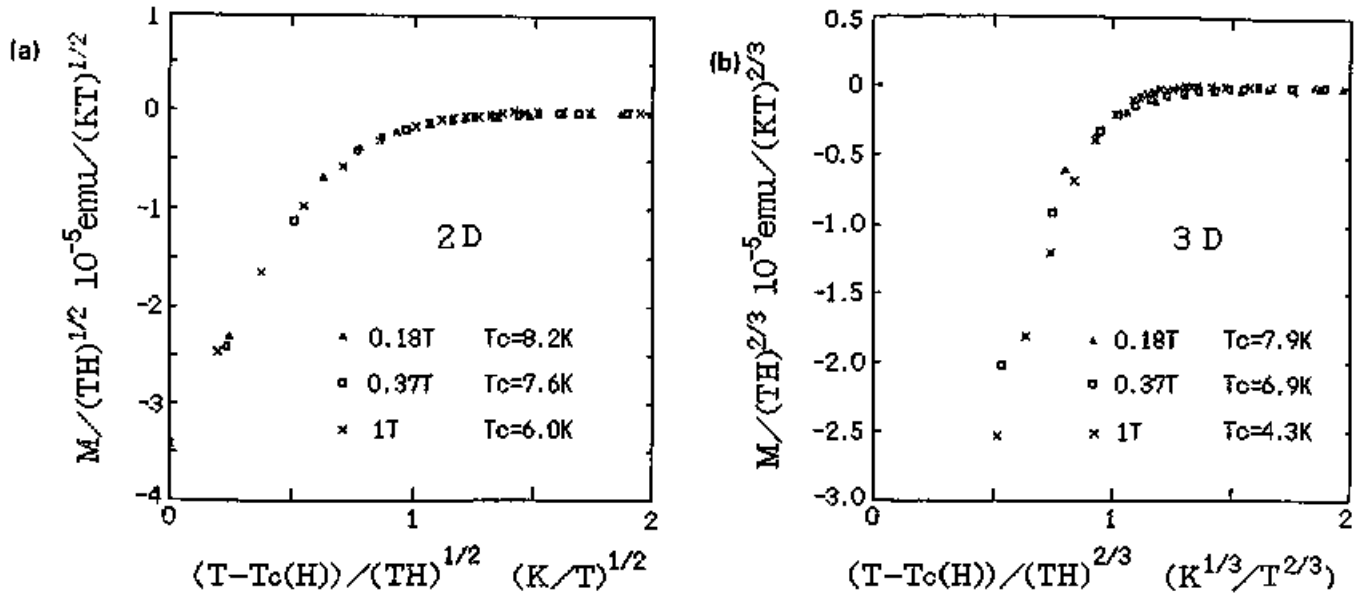
26

Figure 3.7: Field-scaling fit of the magnetization M around the transition region for κ-(h$_8$-BEDT-TTF)$_2$Cu(NCS)$_2$. (a) for 2D scaling and (b) for 3D scaling.
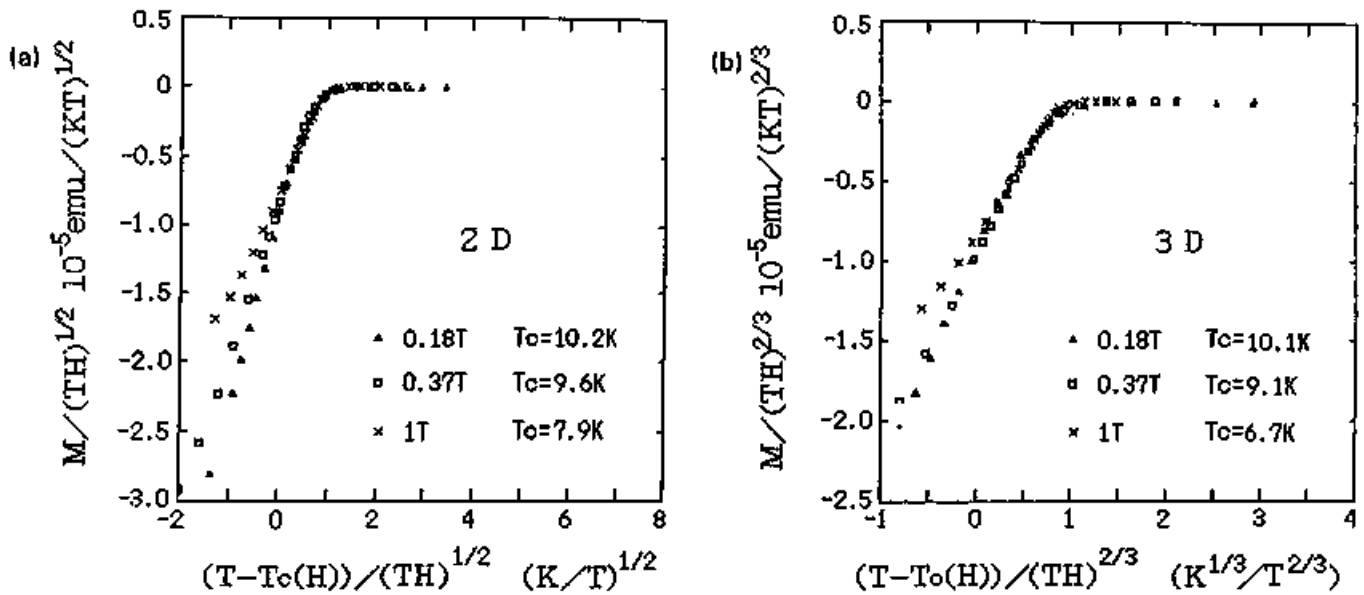

Figure 3.8: Field-scaling fit of the magnetization M around the transition region for κ-(h$_8$-BEDT-TTF)$_2$Cu[N(CN)$_2$]Br. (a) for 2D scaling and (b) for 3D scaling.
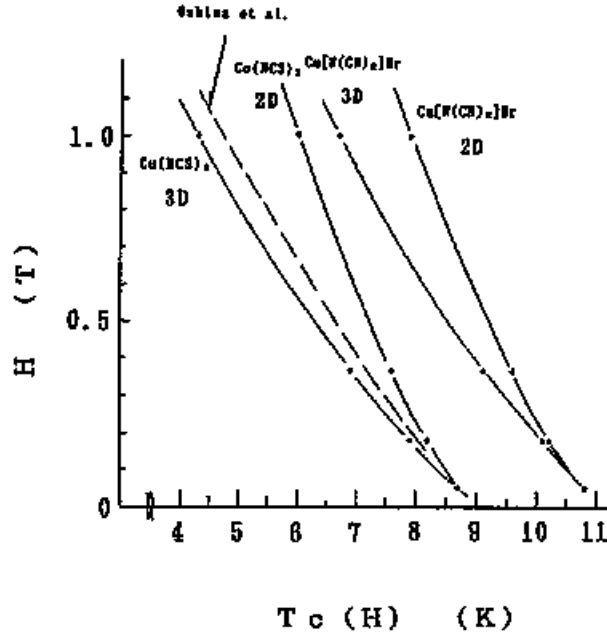
Figure 3.9: Temperature dependence of the upper critical field $H_{c2}(T)$ for κ-(h_8-BEDT-TTF)$_2$Cu(NCS)$_2$ and κ-(h_8-BEDT-TTF)$_2$Cu[N(CN)$_2$]Br obtained by the scaling analysis of magnetization as shown in Figs. 3.7 and 3.8. The $H_{c2}(T)$ line reported by Oshima *et al.* is shown by a broken line.

on the same materials by the other authors [43]. The similar temperature dependence, upward curvature, is reported.

3.6 Concluding Remarks of Chapter 3

In this chapter, the observed temperature and magnetic field dependences of the magnetization are analyzed with respect to the renormalized theory of superconductivity fluctuation. The broad diamagnetic transition under magnetic field is ascribed to the enhanced fluctuation effects of the layered superconductor by a magnetic field.

Along the analysis, the interplane and intraplane superconductivity coherence lengths for κ-(BEDT-TTF)$_2$Cu(NCS)$_2$ and κ-(BEDT-TTF)$_2$Cu[N(CN)$_2$]Br are obtained. We assert that this is the first deduction of the coherence length for the organic superconductor on the sound physical basis, taking account of the low-dimensionality and the high-T_c. It is demonstrated that the interplane coherence length is shorter than the interplane spacing. This indicates that the superconductivity of κ-type BEDT-TTF salts is 2D, which can be properly treated within the framework of the Lawrence-Doniach model. The coherence lengths are found to be insensitive to the isotope substitution of BEDT-TTF molecules in spite of the definite shift in T_c.

28

Since the analytical theory we adopted here is rather universal one, this method can be utilized to analyze the diamagnetic transition of other materials with appropriate fitting parameters. For example, the 3D limit of (3.14) is used to analyze the alkali-doped fullerene superconductors, K_3C_{60} and Rb_3C_{60} [44]. The coherence lengths obtained are 2.1 ± 0.1 nm for the former and 1.3 ± 0.1 nm for the latter. This value implies that the T_c of A_3C_{60} is hitting the ceiling at $T_c = 33$ K for Cs_2RbC_{60} due to the shortness of the coherence length approaching the distance between C_{60} molecules.

Chapter 4

Resistivity Transition under Magnetic Field

In this chapter, we describe the resistive superconductivity transition of κ-type BEDT-TTF salts under magnetic field. The effects of the superconductivity fluctuation and the fluxoid depinning are discussed. In the case of κ-(BEDT-TTF)$_2$Cu(NCS)$_2$, the anomalous resistivity peak below T_c is observed under moderate magnetic fields. This 'resistivity upturn' effect is found to be inherent for the interplane conduction and is discussed in terms of the weak-coupling between 2D superconducting layers.

4.1 Experimental Procedure

The *dc* resistivity has been measured by the standard *dc* four-probe method with measuring current of 0.1-0.2 mA. In this current region the voltage-current relation has been linear for all temperature and magnetic field region studied, within the accuracy of the voltmeter ($\sim$ 10 nV) used for the measurement. For the in-plane resistivity measurement, four electrodes are formed by the gold wires attached onto evaporated gold pads with gold paste (Tokuriki No.8556) as shown in Fig. 4.1(a). For the interplane resistivity measurement, two electrodes are attached on the top and bottom of the conducting crystal plane. We used a special electrode pattern to ensure the equipotential plane parallel to the sample surfaces, as shown in Fig. 4.1(b). In the case of κ-(BEDT-TTF)$_2$Cu(NCS)$_2$, the use of high quality defect-reduced samples is essential to extract the intrinsic transition characteristics. We used the crystals grown by the current-regulation method described in Chapter 2.

To understand the resistive transition characteristics through the theoretical analysis, we consider that it is important to eliminate the effect of local strain accompanying the paste contact. In order to evaluate the strain effect we dare to adopt the wire-contact method in a similar way

(a)
Au film
Au paste
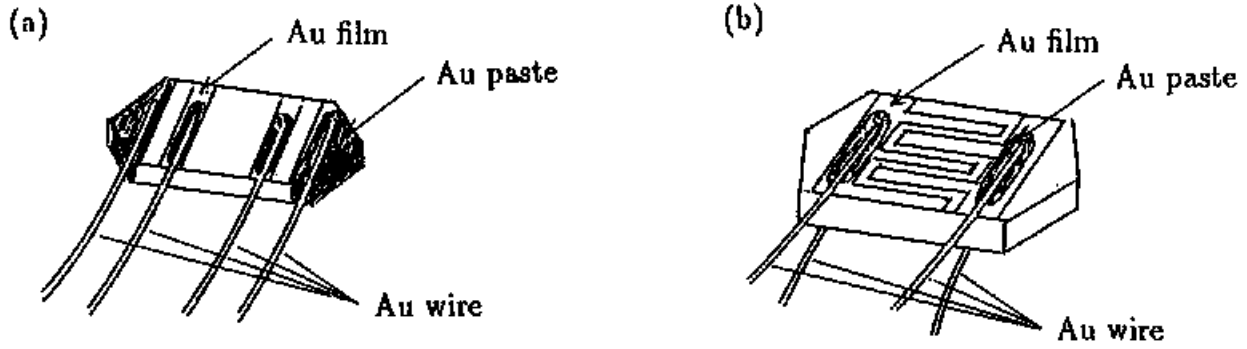Au wire

(b)
Au film
Au paste
Au wire

Figure 4.1: The configuration of the electrodes for the measurement of in-plane (a) and interplane (b) resistivity. For the interplane resistivity, we used special electrode pattern to ensure the equipotential plane parallel to the sample surfaces.

Pt wire
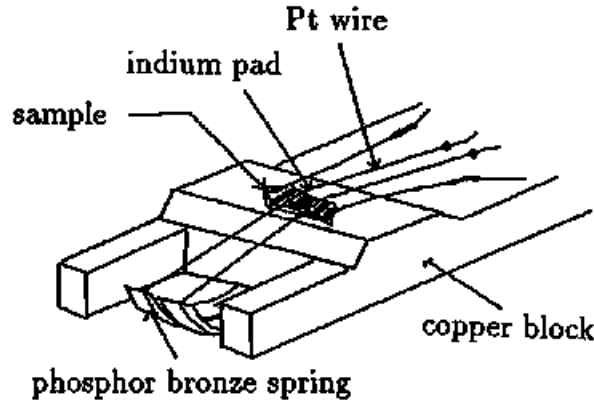indium pad
sample
copper block
phosphor bronze spring

Figure 4.2: The strain-free resistivity measurement using the wire-clamp method. The case for the in-plane measurement is shown.

as applied to TMTSF salt [45] or β-(BEDT-TTF)$_2$I$_3$ [46]. The configuration of electrodes for the in-plane resistivity measurement is shown in Fig. 4.2. The Pt wires of 30 μm are contacted softly just onto the evaporated gold films to form voltage electrodes. Tensile force is given to the wire by using a phosphor bronze spring. A part of the Pt wire is coated by an indium pad to ensure the contact. We consider that the effect of strain from the current electrodes is not serious if there is enough distance from the voltage electrodes. Therefore we apply the paste contact to the current electrodes.

We measured the in-plane and interplane resistivities of κ-(BEDT-TTF)$_2$Cu[N(CN)$_2$]Br in this method around the transition temperature region under the magnetic field perpendicular to the 2D plane. After this measurement we repeated the same measurement with the conventional method

31

method using gold paste to evaluate the effect of the local strain upon the resistivity broadening. Then we found that the difference in the resistivity between two measurements is rather small and almost negligible. Thus we conclude that the use of the paste electrode is justified with respect to the strain, at least in the case of the gold paste which we used.

4.2   Experimental Results

4.2.1 κ-(BEDT-TTF)$_2$Cu[N(CN)$_2$]Br

The temperature dependences of the resistivity of κ-(BEDT-TTF)$_2$Cu[N(CN)$_2$]Br for in-plane (a) and interplane (b) direction under magnetic field perpendicular to the 2D plane are shown in Figs. 4.3(a) and 4.3(b). Clear fan-shaped broadening of resistivity is observed for both cases in the field region of 0 to 1 T. Above 2 T, the transition becomes sharp again in the low temperature region. The resistivity decrease caused by the superconductivity is almost suppressed at 10 T. The transition behaviors for two current configurations look alike. Although the onset and offset temperatures of the transition coincides for two cases, the temperature dependences are slightly different between the two limiting temperatures.
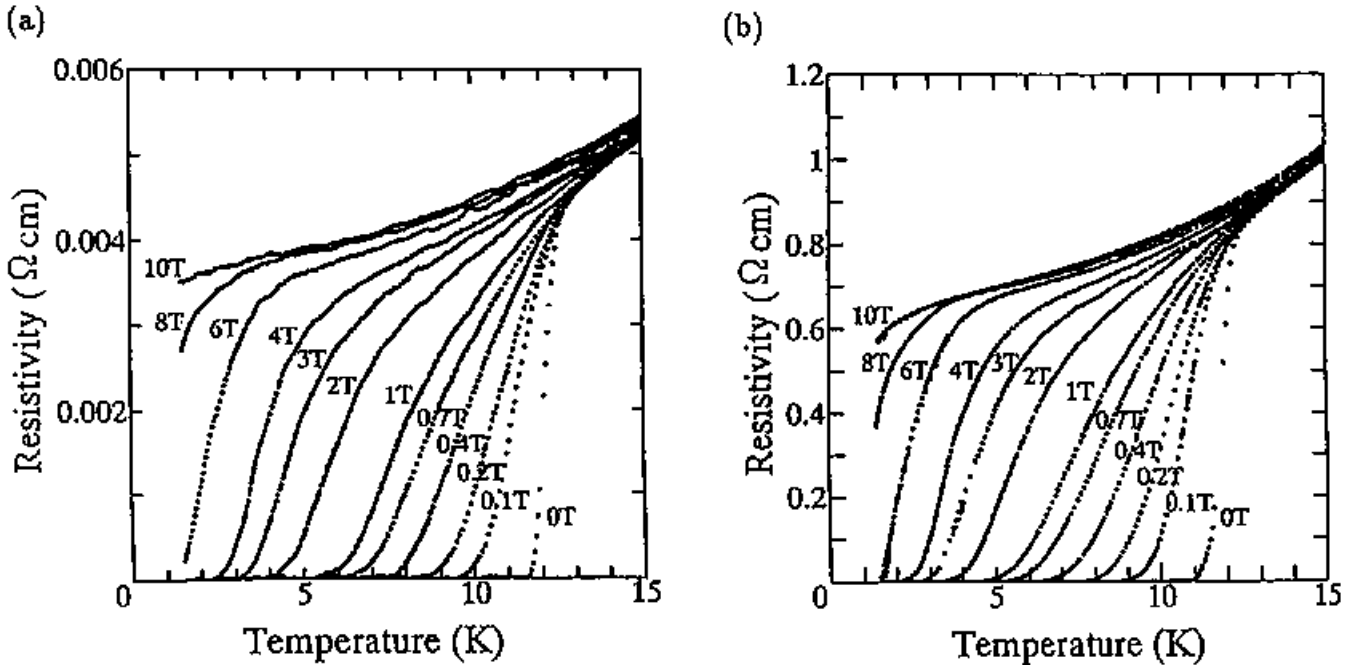
(a)   (b)

Figure 4.3: The temperature dependence of resistivity of κ-(BEDT-TTF)$_2$Cu[N(CN)$_2$]Br for in-plane (a) and interplane (b) direction under magnetic field perpendicular to the 2D plane.

For κ-(BEDT-TTF)$_2$Cu[N(CN)$_2$]Cl, the similar resistive transition broadening under magnetic field is found in the superconductivity state between $T_{c1}\sim$13 K and $T_{c2}\sim$6.7 K, stabilized under applied hydrostatic pressure [13].

4.2.2 κ-(BEDT-TTF)$_2$CuCN[N(CN)$_2$]

The temperature dependence of resistivity for κ-(BEDT-TTF)$_2$CuCN[N(CN)$_2$] is shown for in-plane current direction in Fig. 4.4. The behavior is similar as the κ-(BEDT-TTF)$_2$Cu[N(CN)$_2$]Br. The temperature and magnetic field range of the transition characteristics are smaller for this salt than for the former. The only difference is the small negative magnetoresistance above 5 T [47] which is illustrated in Fig. 4.5 as the field dependence of resistivity. It can be interpreted as a weak localization effect, or may come from the weak-coupling effect discussed in §4.3.3.

4.2.3 κ-(BEDT-TTF)$_2$Cu(NCS)$_2$

For κ-(BEDT-TTF)$_2$Cu(NCS)$_2$, the width of the superconductivity transition between the onset and the offset of the resistivity change is larger than the other salt, $\sim$ 1 K, at zero external magnetic field. We can point out the possibility of the Kosterlitz-Thouless transition related to the unbinding of vortex and anti-vortex pairs in 2D superconductors, which is suggested to occur in strong 2D salts, such as α-(BEDT-TTF)$_2$NH$_4$Hg(SCN)$_4$ [48]. Here, however, the effect of T_c distribution in the crystal due to the inhomogeneiety cannot be ruled out.

Under the magnetic field up to 4 T, the resistivity exhibits anomalous upturn below T_c at zero field (T_{c0}) unlike the other two salts. The behavior of the in-plane resistivity in a magnetic field perpendicular to the 2D plane of a single crystal grown by the conventional constant-current method is shown in Fig. 4.6. The resistivity upturn grows with the increase of magnetic field up to 2T, but it turn to reduce above 3 T and eventually vanishes at 6 T, in accordance with the suppression of superconductivity. Above 6 T, the resistivity exhibits monotonous positive magnetoresistance. The results for the defect-reduced single crystals grown by the current-regulation method are shown in Figs. 4.7(a) and 4.7(b) for in-plane (a) and interplane (b) cases, respectively. In this case, the anomalous resistance upturn vanishes for the in-plane resistivity, while it still exists in the interplane resistivity.
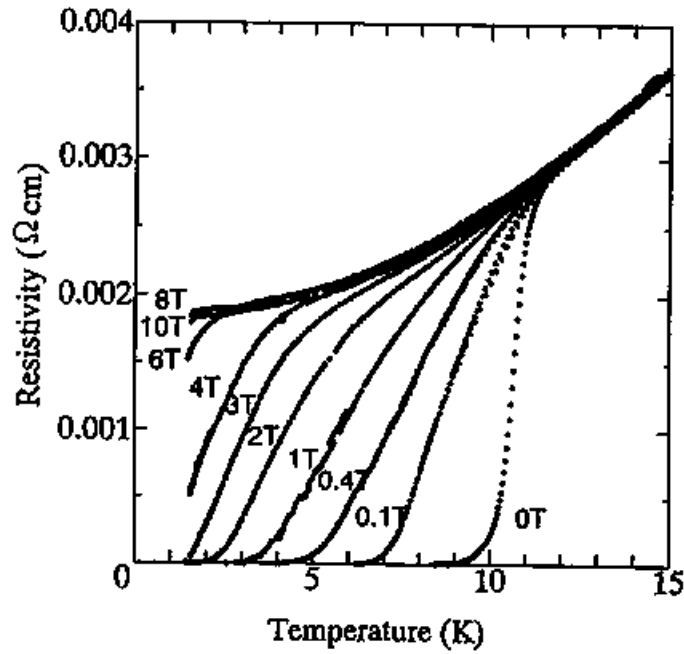
Figure 4.4: The temperature dependence of resistivity of κ-(BEDT-TTF)$_2$CuCN[N(CN)$_2$] for in-plane direction under magnetic field perpendicular to the 2D plane.
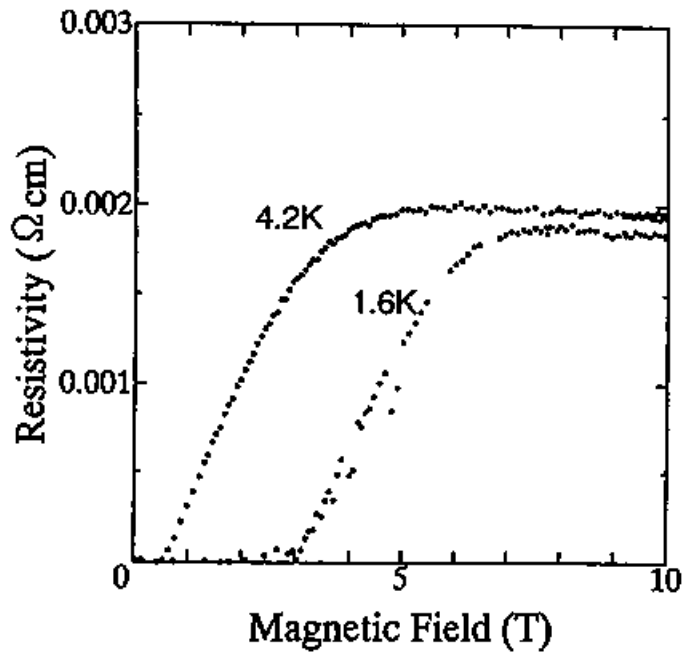

Figure 4.5: The magnetic field dependence of resistivity for κ-(BEDT-TTF)$_2$CuCN[N(CN)$_2$] at 4.2 K and 1.4 K. Small negative magnetoresistance appears above 5 T.
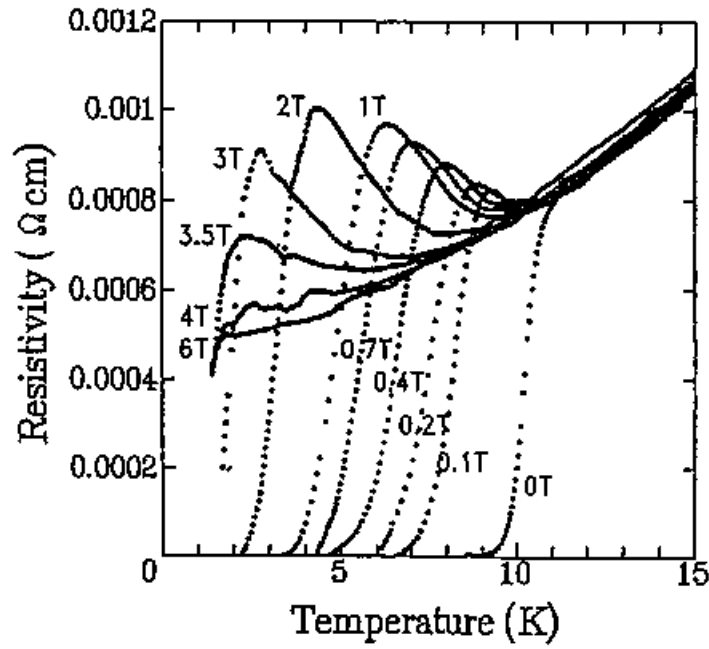
34

Figure 4.6: The temperature dependence of the in-plane resistivity under magnetic field perpendicular to the 2D plane for κ-(BEDT-TTF)$_2$Cu(NCS)$_2$ crystal grown by conventional constant-current method.
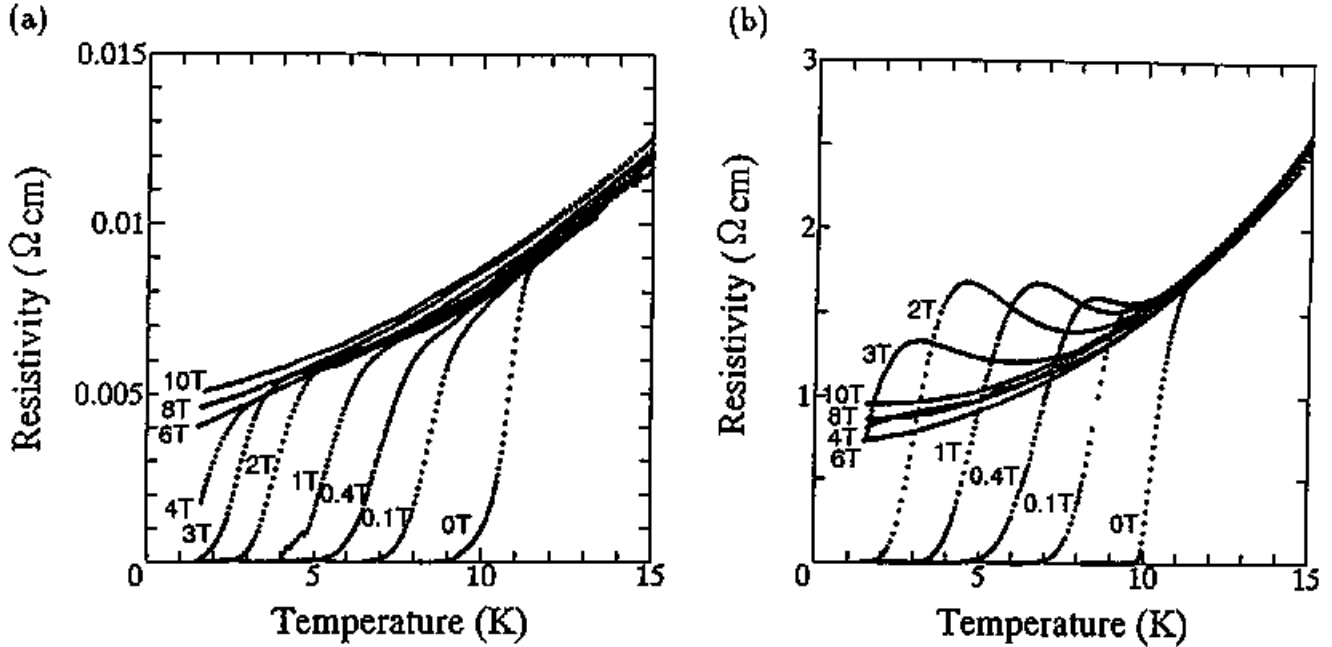
(a)

(b)

Figure 4.7: The temperature dependence of the in-plane (a) and interplane (b) resistivity, under magnetic field perpendicular to the 2D plane, for high quality κ-(BEDT-TTF)$_2$Cu(NCS)$_2$ crystal grown by the current-regulation method.
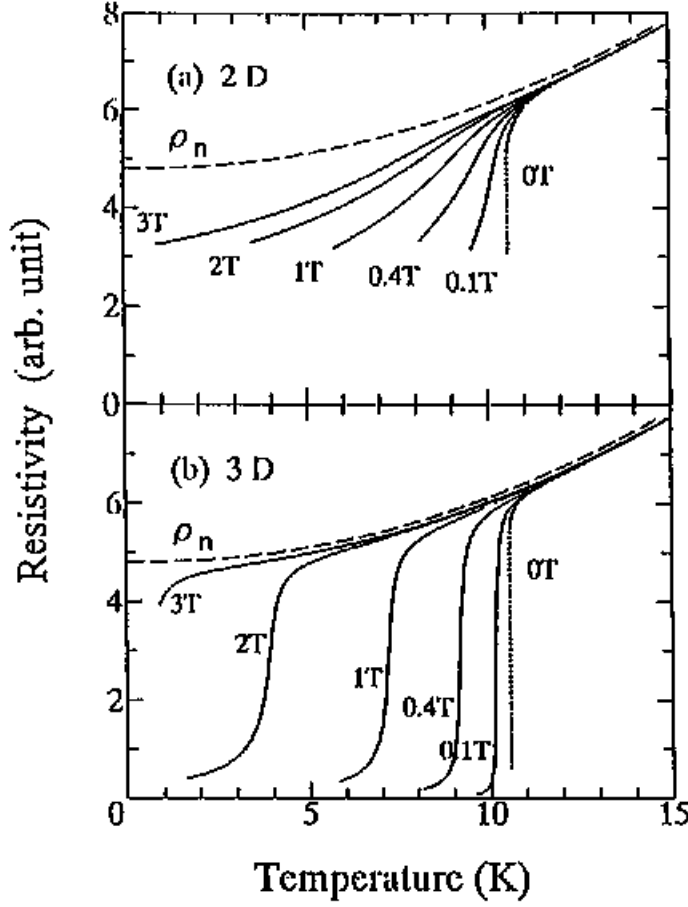
Figure 4.8: Calculated typical in-plane resistivity in magnetic fields perpendicular to the 2D plane for (a) the fluctuation-dominated 2D and (b) the mean field 3 D cases. In the 2D case the zero resistivity is achieved under the presence of fluxoid pinning. Calculations are carried out by (4.1) with the intraplane conductivity formula (3.5). The parameters used are as follows, $\xi_\perp = 0.12$ nm, $\xi_\parallel$=3.7 nm and $C = 300$ for 2D and $\xi_\perp = \xi_\parallel = 10$ nm and $C = 10$ for 3D. Other parameters T_{c0}=10.5 K, ΔC=520 mJ/K·mol and d=1.52 nm are common to both cases.

4.3   Discussion

4.3.1   Effect of superconductivity fluctuation

The fan-shaped broadenings of the resistivity in the 2D superconductors are explained mainly by the thermal fluctuation effect in the case of the cuprate superconductors, such as YBa$_2$Cu$_3$O$_7$ and Bi$_2$Sr$_2$CaCu$_2$O$_8$ [29]. In the renormalized fluctuation theory described in Chapter 3, the resistivity is written as [49],

$$\rho(T) = \frac{1}{\frac{1}{\rho_n(T)} + \frac{\sigma_s(B,T)}{C}} , \tag{4.1}$$

where $\rho_n(T)$ is the normal resistivity as a function of T and C is a parameter to deal with the

36

uncertainty of the normal resistivity. For the parameter C, it is reasonable to fall in a range of the order of 0.1 to 10, according to the geometrical restriction for the electrode with respect to the sample size and shape. For the superconductivity contribution $\sigma_s(B,T)$ to the conductivity, we use (3.5) for the in-plane and (3.11) for the interplane current direction with appropriate renormalized mass parameters $\mu_{nR}(B,T)$. Figure 4.8 illustrates the typical temperature dependences of the in-plane resistivity in a magnetic field normal to the conducting plane, for a fluctuation dominated 2D case (a) and for a mean field 3D case (b) calculated by (4.1). The 2D and the 3D cases correspond to those with $\xi_\perp < d$ or $\xi_\perp > d$, respectively. In the 2D case, the resistivity does not reach zero down to low temperature. This is because the theory presumes the quasi-static fluxoids flow under the magnetic field [50]. While in the real superconductor, since the fluxoid flow is hindered by the pinning at defects and/or by the phase transition of fluxoid system to the glass state, the resistivity becomes zero even in the presence of a magnetic field.

In the case of κ-(BEDT-TTF)$_2$Cu[N(CN)$_2$]Br, the fan-shaped broadening of the resistivity below 1 T may be ascribed to the thermal fluctuation effect. We explain the data shown in Figs. 4.3(a) and 4.3(b) with respect to the renormalized fluctuation theory presented in Chapter 3. First we deal with the case when the current is parallel to the field, i.e., the interplane resistivity under the magnetic field perpendicular to the 2D plane, since we expect smaller contribution of the fluxoid flow than in the case of the in-plane resistivity. The normal resistivity $\rho_n(T)$ is evaluated by a smooth extrapolation of the resistivity curve from the temperature region above T_c obeying T^2-law. With the values of $\xi_\perp=0.4$ nm and $\xi_\parallel=2$ nm, which are close to those deduced by the analysis of the dc magnetization in Chapter 3, we get an acceptable fitting as shown in Fig. 4.9(a) by using a value of $C = 3.0 \times 10^3$ This C value is very large compared to the expected one of the order 0.1 to 10. If we reduce the value, $e.g.$, to unity while keeping the coherence lengths unchanged, the broadening of the transition becomes very weak and almost negligible. Here we remark that if we use smaller $\xi_\perp$ and larger $\xi_\parallel$, the C value can be decreased without reducing the transition width, although this set of the coherence lengths does not reproduce the observed dc magnetization shown in Fig. 3.2. In Fig 4.9(b), we show a fitting example with a set of parameters as $\xi_\perp=0.12$ nm, $\xi_\parallel=3.7$ nm and $C=11.5$.

For the in-plane resistivity we get best fitted lines with the values near $\xi_\perp=0.12$ nm and $\xi_\parallel=3.7$ nm and $C = 3.0 \times 10^2$ as shown in Fig. 4.10. The calculated resistive transition is much broader
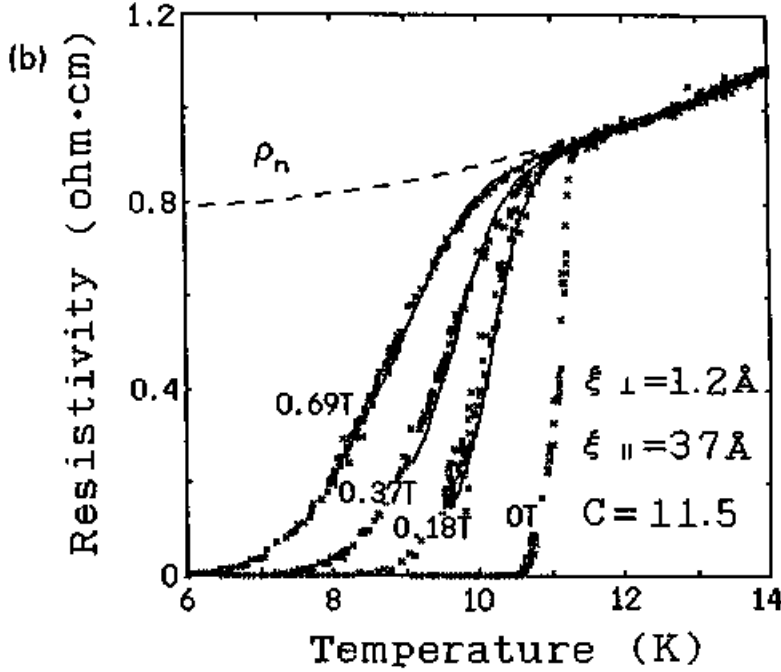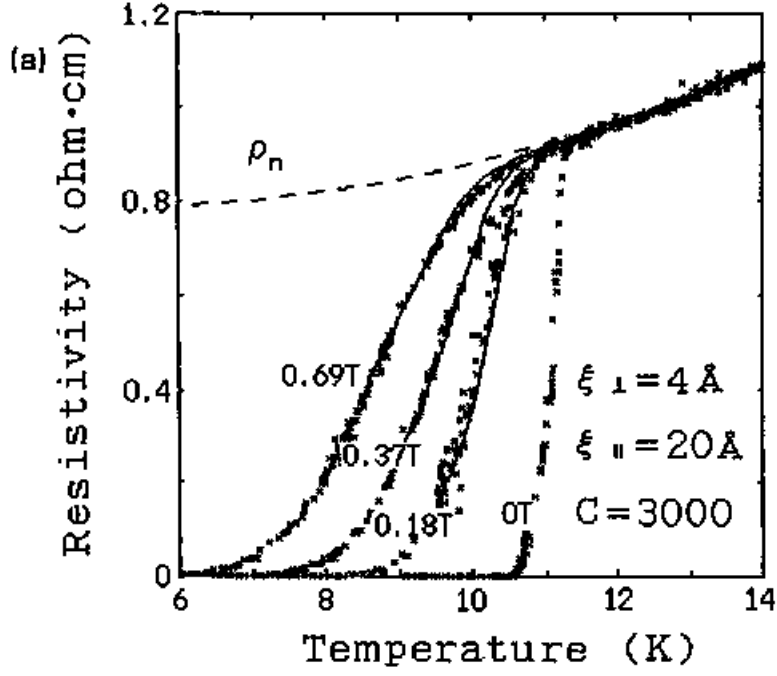
Figure 4.9: The fitting of the interplane resistivity of κ-(BEDT-TTF)$_2$Cu[N(CN)$_2$]Br to the renormalized fluctuation theory in the magnetic field region up to 0.69 T. The used parameters are $\xi_\perp$=0.4 nm, $\xi_\parallel$=2 nm and $C = 3.0 \times 10^3$ for (a). If we set $C = 1$, the broadening effect becomes negligibly small. When we use a set of coherence lengths, $\xi_\perp$=0.12 nm and $\xi_\parallel$=3.7 nm, C can be reduced to 11.5 keeping the broadening feature unchanged, as shown in (b). Here, the other parameters are the same as the analysis of the dc magnetization in Chapter 3, i.e., T_{c0}=10.9 K, ΔC=520 mJ/K·mol and d=1.52 nm.
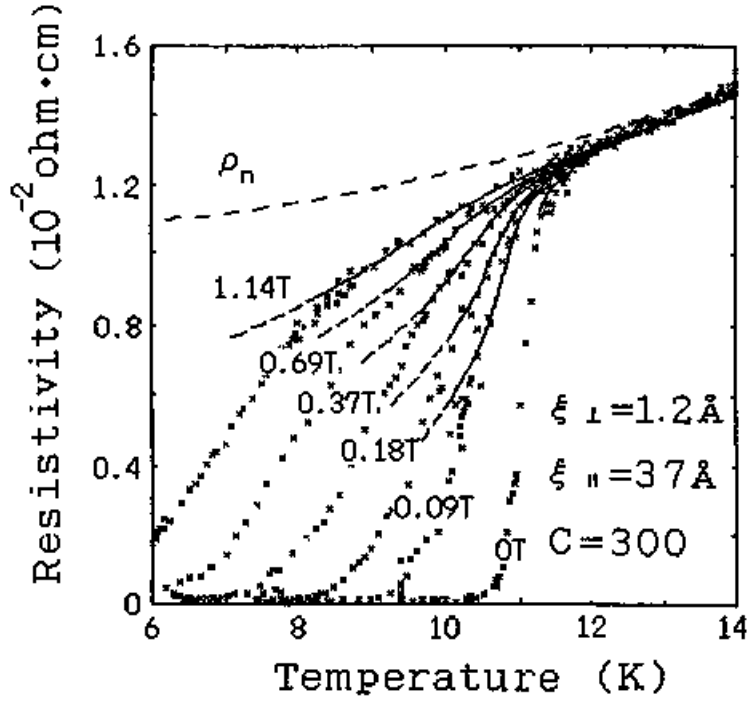
Figure 4.10: The fitting of the in-plane resistivity of κ-(BEDT-TTF)$_2$Cu[N(CN)$_2$]Br to the renormalized fluctuation theory in the magnetic field region up to 1.14 T. The used parameters are $\xi_\perp$=0.12 nm, $\xi_\parallel$=3.7 nm and $C = 300$. The other parameters are the same as Fig. 4.9.

than that of the interplane resistivity due to the fluxoid flow contribution. With the aid of the fluxoid pinning effects, the resistivity becomes zero.

In the present analysis, we have to use very large C value to get reasonable fit to the theory for both current directions, using the acceptable values of the coherence lengths determined from the analysis of the magnetization. The large C value indicates that the fluctuation contribution to the observed resistivity behavior is less than that expected. This is inconsistent with the result of the dc magnetization, where the behaviors are understood fairly well by the renormalized superconductivity fluctuation theory. As the reason for this discrepancy, we cannot dismiss the approximation for the normal (quasiparticle) contribution in the present calculation. Furthermore, in the case of the transport studies, we must take account of the other contributions to cause dissipations in the mixed state of superconductors. We point out several remarks to understand the observed behaviors of the resistive transition under the magnetic field.

(1) The contribution of the pinning effect and the relevant fluxoid depinning influence the resistivity not only at the offset region of the resistive transition but also at the critical region near T_c. The strong pinning may hinder the quasi-static fluxoid flow. In the case of the interplane resistivity the pinning contribution is expected to be small, while, in the real superconductor, the

current path may not be always perpendicular to the 2D plane. The in-plane contribution can be involved in the interplane resistivity behavior.

(2) The effect of quasiparticle contribution to the resistivity is treated in a simple way in (4.1). In this formula the normal resistivity contribution to the conductivity is treated by rather 'naive' application of the two-fluid model. In other words, we should add the quasiparticle current to the supercurrent formula from the beginning of the theoretical framework.

(3) We cannot neglect the effect of sample inhomogeneity, which is imagined from the dullness of the superconductivity transition even in the absence of the *dc* magnetic field. The inhomogeneiety affects the transport properties more severely than the thermodynamic property such as the magnetization. If the sample is inhomogeneous with respect to T_c, as judged from the transition width of 0.5~1 K at zero magnetic field, some parts of the crystal undergo superconductivity transition while other parts remain to be normal. In such a case, the transition characteristics are dominated by the portion already in the superconductivity state.

(4) The 2D conducting plane, which we have been assumed to be isotropic, is not of complete isotropy. We should take account of the two type of carriers, electrons and holes, as is shown by the calculated Fermi surface in Fig. 1.5.

A part of the discrepancy between the fluctuation theory and the observed resistivity may be ascribed to the above-mentioned points. Among them, the effect of fluxoid dynamics (1) is found to play dominant role on the behavior of resistivity as in §4.3.2. The effect of quasiparticle current contribution (2) will be discussed in §4.3.3, in relation to the weak-coupling effect.

4.3.2 Effect of fluxoid depinning

As is presented in the previous section, the fluxoid pinning plays important role for the resistivity, more than imagined. Since the Lorentz (Magnus) force acting on the fluxoid to generate quasistatic flow is already included in the fluctuation theory, we consider here the effect of the thermally activated depinning of fluxoids on the resistivity. When the fluxoid moves among the pinning sites by the thermally activated hopping, the conductivity due to this process exhibits the activation-type temperature dependence shown as [51],

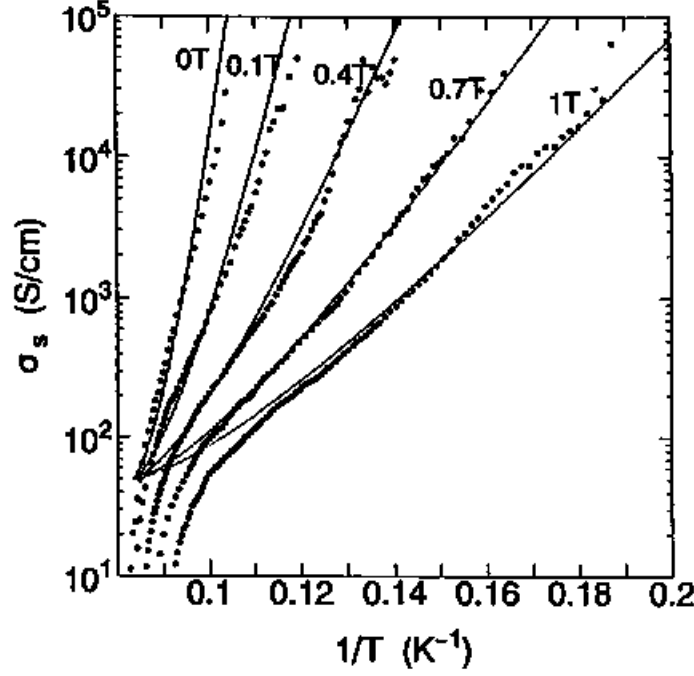$$\sigma_s = \sigma_0 \exp\left(-\frac{U(B,T)}{k_B T}\right), \tag{4.2}$$

Figure 4.11: The Arrhenius plot of the superconductivity contribution to the conductivity σ_s extracted from the data shown in Fig. 4.3(a) up to 1 T. For the normal resistivity, the quadratic fitting of the resistivity data under the magnetic field of 10 T is used.

where σ_0 is a constant. Based on the thermally assisted flux-flow model, the pinning potential $U(B,T)$ is deduced as [52,53],

$$U(B,T) = U_0(1 - t)^{3/2}/B, \qquad (4.3)$$

where t is the reduced temperature defined as $t = T/T_{c0}$. We derive the pinning potential U_0 in (4.3) from the data shown in Fig. 4.3(a) by scaling in a manner of the Arrhenius plot, as shown in Fig. 4.11. The superconductivity contribution to the conductivity σ_s is derived by the subtraction of $1/\rho_n$, which is again evaluated by a smooth extrapolation of the resistivity curve from the temperature region higher than the transition. The vertical axis is scaled by $\log \sigma_s$ and the horizontal by T^{-1} By fitting the conductivity with (4.2) and (4.3), we get the value $U_0 = 7 \pm 1$ meV·T. This value is close to that deduced from the measurement of the magnetization relaxation [54,55]. The present fitting indicates that, at least in the case of the in-plane resistivity, the thermally assisted fluxoid depinning effect dominantly contributes to the resistivity over relatively large temperature and magnetic field region. In Fig. 4.11, the deviation of the observed conductivity from the theoretical one near T_{c0} is considered to be due to the fluctuation effect discussed in the previous section. However, it is difficult to deal with this small

41

deviation quantitatively since the evaluation of the fluctuation conductivity sensitively depends on the normal resistivity for which we must permit some uncertainty.

4.3.3 Effect of weak-coupling

In the case of κ-(BEDT-TTF)$_2$Cu(NCS)$_2$, the interplane resistivity exhibits a peak below T_{c0} in the presence of magnetic field up to 4 T applied perpendicular to the 2D plane. This anomalous resistance upturn of κ-(BEDT-TTF)$_2$Cu(NCS)$_2$ has been pointed out since the very beginning of the study of this salt [56]. At first, some magnetic scattering effect by impurity or due to mixed valence of Cu were proposed, although no sigh for the magnetic order or mixed valence state has been reported so far around the transition region [18–20]. Pratt *et al.* studied this effect in detail and discussed as a negative magnetoresistance effect due to weak localization. However, the magnitude is too large to be ascribed to that [57].

For the better understanding of the effect we pay attention to the fact that it is closely related to the superconductivity of this material. The onset of the resistance upturn coincides with the superconductivity transition temperature and its disappearance in a magnetic field above 6 T again coincides with the suppression of superconductivity. Furthermore, we must take into account the fact that the other κ-type salts do not exhibit the resistance upturn. Enomoto *et al.* found similar resistance upturn effect in the polycrystalline film of Ba$_{1-x}$K$_x$BiO$_3$ [58]. They applied the resistive shunted junction model [59] on the grain boundary Josephson junctions and explained qualitatively the behavior of the resistivity under magnetic fields. In κ-(BEDT-TTF)$_2$Cu(NCS)$_2$ the layered structure is inherently modeled as an array of Josephson junctions [26]. The application of the resistive shunted junction as a model of the interplane conduction of layered superconductors has already been discussed on the cuprate superconductors such as Bi$_2$Sr$_2$CaCu$_2$O$_8$ [60] and La$_{2-x}$Sr$_x$CuO$_4$ [61]. Since the anisotropy of the superconductivity of κ-(BEDT-TTF)$_2$Cu(NCS)$_2$ is stronger than other κ-type salts as shown by the coherence length presented in Chapter 3, the intrinsic junction nature is more dominant for the interplane conduction of this salt.

As for the weak-coupling structure, we also remark the anion stacking fault suggested by Ravy *et al.* [62]. The component of polymeric anion chain can take a configuration of reverse order due to its symmetry (*cf.* Fig. 1.4). This defect disturbs the arrangement of the BEDT-TTF molecules in the conducting plane and creates dislocation which divides the superconducting region into two
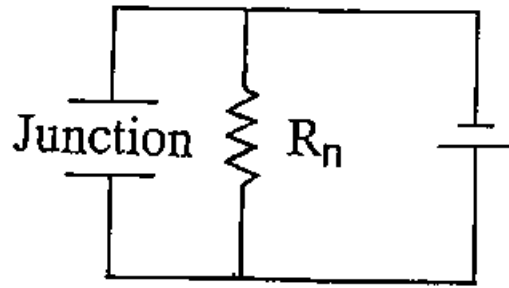
Figure 4.12: The equivalent circuit in the resistive-shunted-junction model.
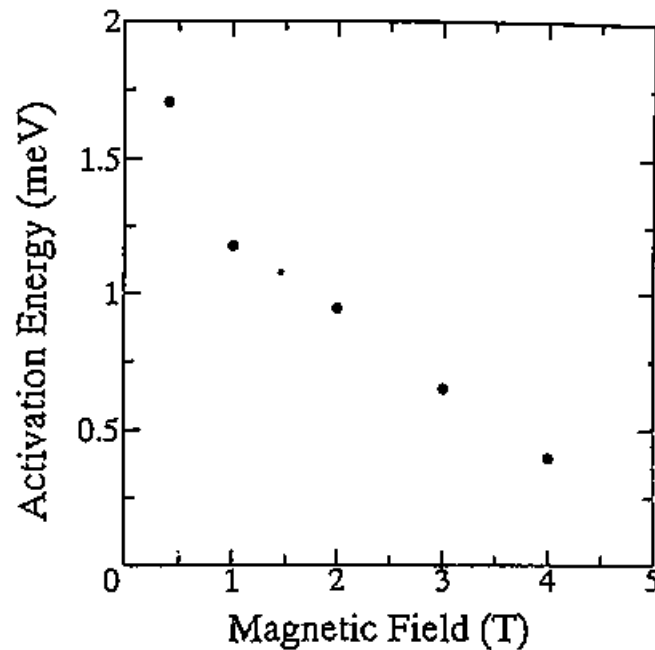

Figure 4.13: The activation energy of the upturn part of the resistivity deduced by the analysis along (4.4).

and produce a junction-like structure. Due to the antisymmetric component of anion polymeric chain, such defect is suppressed for the other salts. This effect influences mainly the in-plane conduction, which may be responsible for the resistance upturn appearing for the sample grown in a conventional method.

In the resistively-shunted-junction model, the junction is modeled as an identical circuit shown is Fig. 4.12. Taking into account the thermal fluctuation around the shunted resistance R_n, the total resistance is formulated as a product of R_n and a function of temperature and magnetic field as,

$$R = R_n \left\{ I_0 \left(\frac{\hbar}{2ek_BT} J_c(0) \left[1 - \frac{T}{T_{c0}} \right]^{3/2} \frac{\phi_0}{H} \right) \right\}^{-2} \tag{4.4}$$

For the shunted resistance we use the resistance for the quasiparticles. It has been modified by the quasiparticle tunneling resistance which is essentially the activation type with the energy related to the superconductivity gap. This picture is supported by the gap formation in the quasiparticle spectrum due to the superconductivity gap 2Δ [63–65]. We deduce the activation energy of the resistivity upturn part from the data of Fig. 4.7(b). The activation energy decreases with the increase of magnetic field as shown in Fig. 4.13. This behavior is consistent with the suppression of superconductivity by a magnetic field. In the zero magnetic field limit the value tends to be 2 meV. This value is rather close to the expected superconductivity gap of $2\Delta = 3.5k_BT_c \simeq 3.1$ meV In this model, the overall behavior of the resistivity is explained by the competition between the quasiparticle current and the supercurrent contributions. At high temperature, the supercurrent across the junction is suppressed by the phase fluctuation between the 2D superconductivity layers on each side of the junction and the resistivity is dominated by the quasiparticle current. On the other hand, in the low temperature side, the supercurrent across the plane begins to flow and the circuit is shorted resulting in the resistivity decrease. This behavior is related to the interplane decoupling effect, as will be discussed in Chapter 5.

In some samples of κ-(BEDT-TTF)$_2$Cu[N(CN)$_2$]Br, we find the resistance peaks as shown in Fig. 4.14. Eventually as an additional character of the sample giving this data, we point out the fact that the superconducting portion estimated from the magnetic shielding measurement is small (the estimated superconducting volume fraction is less than 50%). This indicates that the sample contains considerable amount of the nonsuperconducting portion. Under this situation we imagine that there exist percolation paths invoking the weak-coupling, resulting in the magnetoresistance peaks. Here we notice that the transition behavior shown in Fig 4.14 under a certain magnetic field looks similar to the 3D case shown in Fig. 4.8(b), especially in the low field region. We find however that the intervals between the curves for different fields are quite different between the cases in Fig. 4.8(b) and Fig. 4.14. If we plot the midpoints of the resistive transition, which had been regarded as H_{C2}, they are almost proportional to $T_c - T$ for Fig. 4.8(b), while they show upward curvature for Fig. 4.14 as illustrated in Fig. 4.15, as first pointed out by Oshima *et al.* [36]. Similar remark can be given for the case of high quality sample of κ-(BEDT-TTF)$_2$Cu(NCS)$_2$
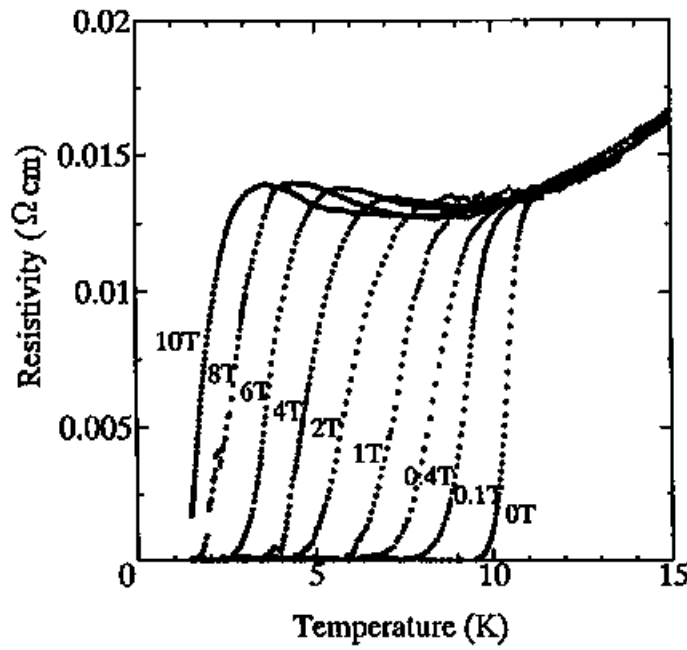
Figure 4.14: The temperature dependence of in-plane resistivity of κ-(BEDT-TTF)$_2$Cu[N(CN)$_2$]Br crystal of inferior quality under magnetic field perpendicular to the 2D plane.
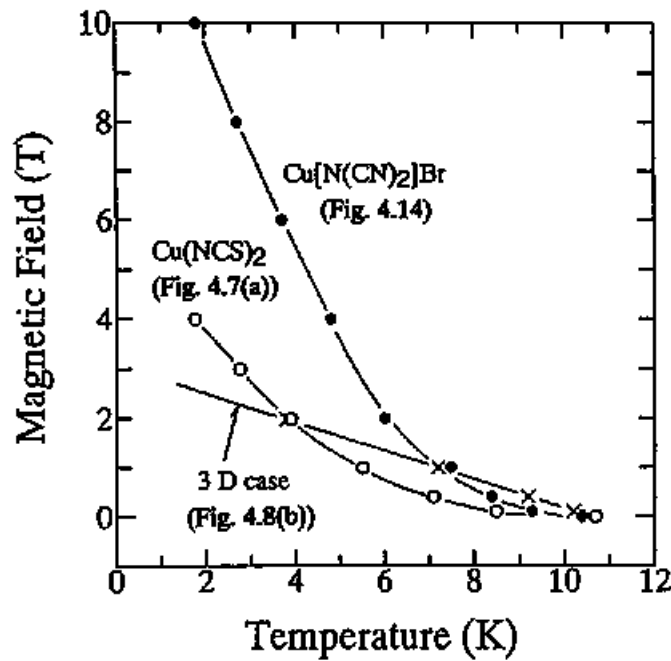

Figure 4.15: Temperature dependence of the magnetic field giving the mid-point value of the resistive transition in Fig. 4.8(b)(cross), Fig. 4.14(closed circle) and Fig. 4.7(a)(open circle). The field corresponds to the conventional H_{C2} value.
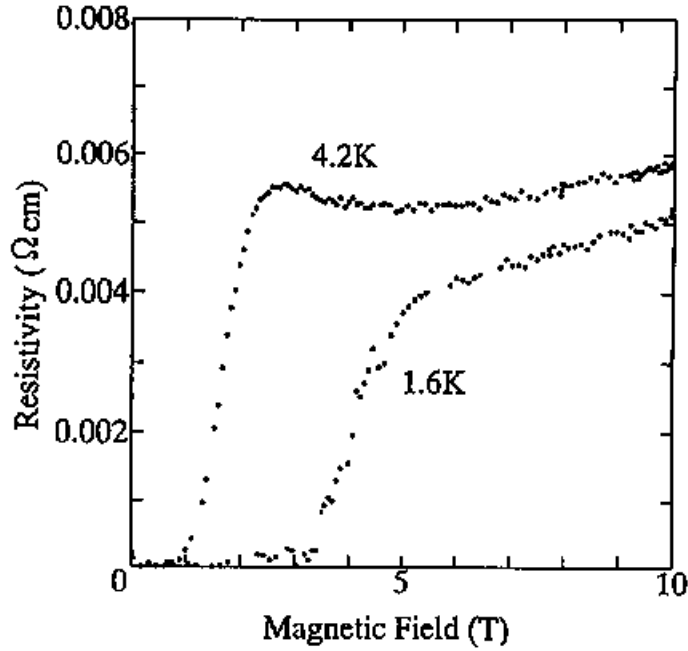
Figure 4.16: The magnetic field dependence of resistivity for the high quality sample of κ-(BEDT-TTF)$_2$Cu(NCS)$_2$ at 4.2 K and 1.4 K. Small negative magnetoresistance appears at 4.2 K.

shown in Fig. 4.7(b). For the latter by inspecting the resistive transition in more detail, we find that the resistance peak retains its trace as shown in Fig. 4.16. This can be understood that even in the *high quality* sample the effects of the weak coupling appearing at defects are not completely ruled out. We consider that a way to explain the behaviors shown in Fig. 4.14 and Fig. 4.7(b) is to take account of the superposition of the weak-coupling effects onto the 2D like fan-shaped transition in the presence of the fluxoid pinning. It is understood that the transport characteristics are more influenced by the sample inhomogeneity than the thermodynamic ones : the resistance is determined by percolation paths representing the characteristics of limited parts of a sample. The variety in the resistive transition has been considered to arise from this complexity.

4.4 Concluding Remarks of Chapter 4

The temperature and magnetic field dependence of resistivity around the superconductivity transition is discussed in terms of the superconductivity fluctuation and the fluxoid pinning. Near the transition the effect of superconductivity fluctuation is dominant, while in the low-temperature region the effect of thermally assisted fluxoid flow becomes significant.

For κ-(BEDT-TTF)$_2$Cu(NCS)$_2$, the nature of the weak-coupling between 2D superconducting plane dominates the transition characteristics. The anomalous resistivity peak under the magnetic

46

field is ascribed to the competition between the activation-type quasiparticle resistance and the supercurrent. In the case of samples with inferior quality, the effect of weak-coupling across the defects often influences on the resistivity behavior. We propose a clue to dissolve the problem in view of the contribution from the weak-coupling appearing at the boundaries of the superconducting region, distributing in inhomogeneous samples. To quote the intrinsic resistive transition behavior, comprehensive studies including the characterization on the sample crystalinity are needed.

Chapter 5

ac Magnetic Susceptibility under Magnetic Field

As is discussed in the previous chapter, the effect of the fluxoid dynamics cannot be neglected in addition to the thermal fluctuation to understand the transition characteristics in the presence of magnetic field. In this chapter we throw attention to the dynamics and structure of the fluxoid system in the mixed state of κ-type BEDT-TTF salts, through the ac susceptibility measurement under an external dc magnetic field. We present the frequency and orientation dependences of the ac magnetic susceptibility under dc magnetic fields applied perpendicular to the 2D plane investigated on κ-(BEDT-TTF)$_2$Cu[N(CN)$_2$]Br. Since similar frequency and orientation dependences are also observed for cuprate 2D superconductor Bi$_2$Sr$_2$CaCu$_2$O$_8$[66], the observed characteristics are common for the layered superconductors and must be interpreted in relation to the 2D nature of the superconductivity transition.

5.1 Experimental Procedure

The magnetic susceptibility at radio-frequency (rf) was obtained from a shift of the inductance of a detection coil containing a single crystal, by measuring the resonance frequency of an LC circuit shown in Fig. 5.1(a). The crystal was set, by paying attention to the alignment with respect to the ac field direction, as shown in Fig. 5.1(b). All of the devices constructing a resonance circuit were set in a cryostat [67]. The uncertainty of the resonance frequency was in the order of ppm. The real part of the susceptibility change due to the superconductivity was extracted by subtracting background signal, which was evaluated by a linear extrapolation of the normal state value appearing above T_c. The shift associated with the superconducting transition reached 1% in the case of the ac field applied perpendicular to the crystal plane. For the ac field applied parallel to the plane, the signal level was about a half of that for the ac field perpendicular to the
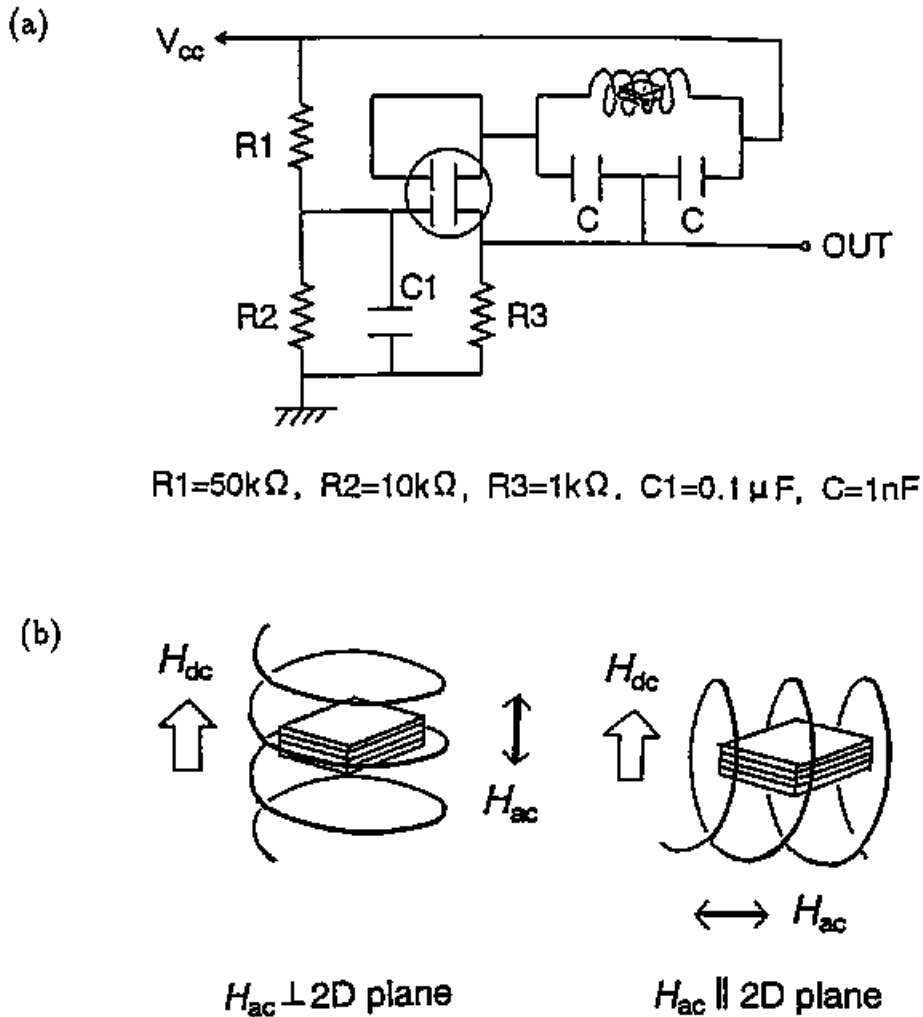
(a)

V_{cc}

R1   R2   R3   C1   C

R1=50kΩ, R2=10kΩ, R3=1kΩ, C1=0.1μF, C=1nF

(b)

H_{dc} H_{ac} H_{dc} H_{ac}

$H_{ac} \perp$ 2D plane $H_{ac} \parallel$ 2D plane

Figure 5.1: The electronic circuit for the radio-frequency ac susceptibility measurement (a). The orientations of the ac magnetic field (H_{ac}) and the dc magnetic field (H_{dc}) with respect to the 2D crystal plane (b).

plane. This difference is ascribed to the sample cross-section in the field direction. The evaluated amplitude of the ac field was ~ 1 μT during the measurement. The external dc magnetic field was generated by a rotatable electromagnet so that the direction of the dc field can be controlled. The data for κ-(BEDT-TTF)$_2$Cu[N(CN)$_2$]Cl were obtained by setting the detection coil inside a pressure cell connected to a He gas pressure generator.

The real and imaginary parts of the ac magnetic susceptibility, at frequencies lower than 1 kHz, were measured by using a SQUID magnetometer equipped with an ac modulation option. In this measurement both ac and dc fields were applied perpendicular to the crystal plane. The amplitude of the ac field was set to ~ 1 μT.

At the intermediate frequency of 10 kHz and 100 kHz, the real and imaginary parts of *ac* susceptibility were measured by a conventional mutual-inductance method. The *ac* field was applied by an excitation coil. In-phase and out-of-phase *ac* voltages concerning the change in the susceptibility of sample were detected by a pick-up coil, which was wound coaxially inside the excitation coil. To get enough signal, the amplitude of the *ac* magnetic field must be set to the order of 0.1 mT, which is two order of magnitude larger than in the cases for other frequencies. However, the susceptibility data can be discussed on the same regime as that at other frequencies, i.e., in the linear regime, since the susceptibility signal was proportional to the magnitude of applied *ac* field in the range from 0.05 mT to 0.2 mT.

5.2 Experimental Results

5.2.1 κ-(BEDT-TTF)$_2$Cu[N(CN)$_2$]Br

The temperature dependences of the real part of the magnetic susceptibility of κ-(BEDT-TTF)$_2$Cu[N(CN)$_2$]Br under *dc* magnetic field are shown in Figs. 5.2(a), 5.2(b), 5.2(c), 5.2(d) and 5.2(e). In these cases both of the *ac* field and *dc* field were applied perpendicular to the 2D crystal plane. The frequencies used were 17 Hz (Fig. 5.2(a)), 997 Hz (Fig. 5.2(b)), 10 kHz (Fig. 5.2(c)), 100 kHz (Fig. 5.2(d)) and 3.2±0.05 MHz (Fig. 5.2(e)). At 17 Hz, the onset of flux expulsion shifts to lower temperature with the increase of *dc* magnetic field, without changing the transition width. On the other hand, at 3.2 MHz the onset temperature of the flux expulsion hardly changes while the diamagnetic transition is broaden with the increase of the *dc* magnetic field. In the intermediate frequency region, 997 Hz, 10 kHz and 100 kHz as shown in Figs. 5.2(b~d), the transition behavior is similar to the case for 17 Hz, although the transition width increases with the increase of the *dc* magnetic field and shows the tendency of the broadening like the case of 3.2 MHz, as the frequency increases. We note that the onset temperature of the diamagnetic transition greatly depends upon frequency, but the offset temperature of the transition is found in the similar temperature region for all frequencies investigated.

The imaginary parts of the susceptibility at 17 Hz, 997 Hz, 10 kHz and 100 kHz are shown in Figs. 5.3(a), 5.3(b), 5.3(c) and 5.3(d). The onset of the imaginary part coincides with that of the diamagnetic transition appearing in the real part. The peak of the imaginary part corresponds to the steepest change of the real part in the transition region. Near the offset temperature of
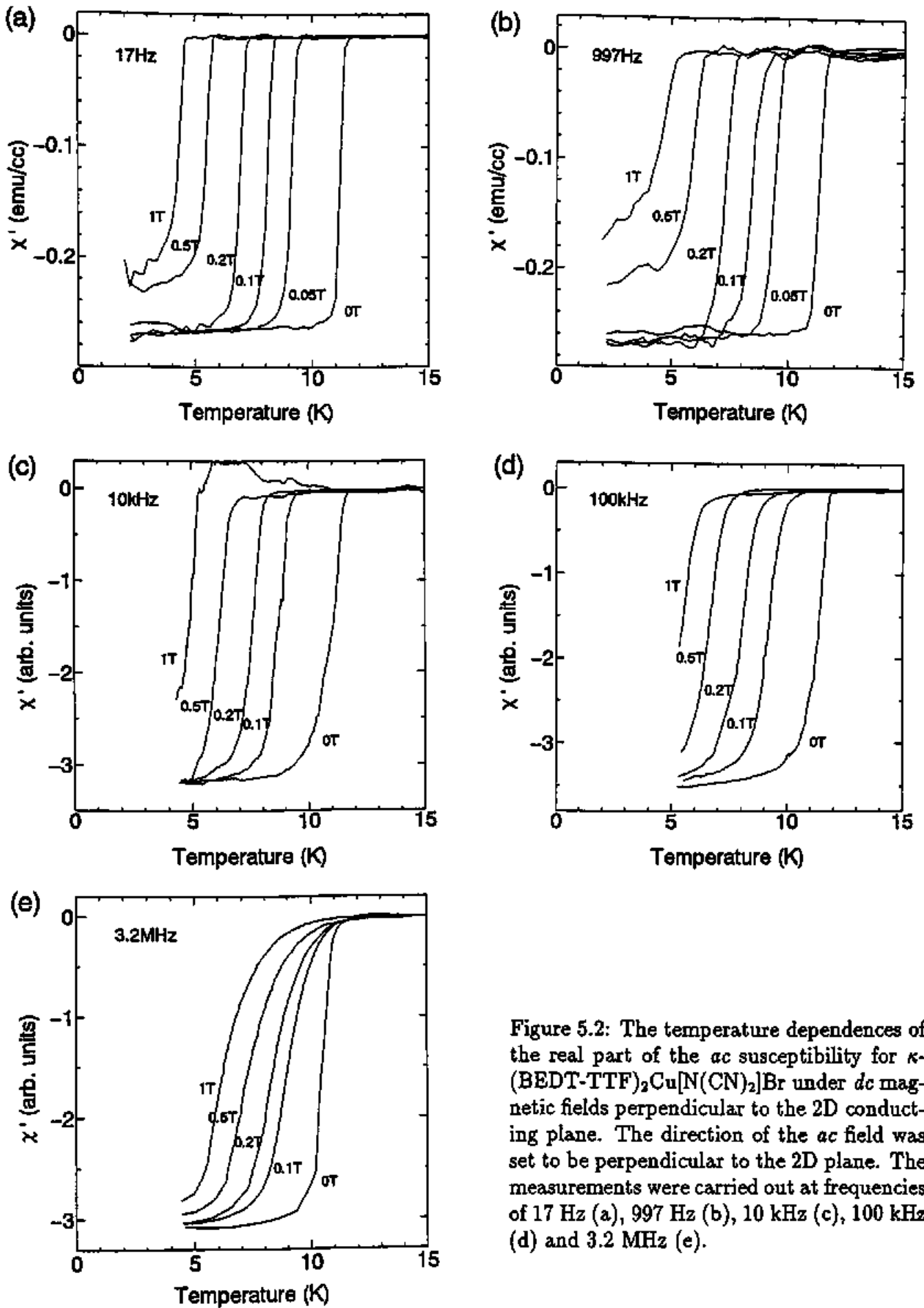
Figure 5.2: The temperature dependences of the real part of the ac susceptibility for κ-(BEDT-TTF)$_2$Cu[N(CN)$_2$]Br under dc magnetic fields perpendicular to the 2D conducting plane. The direction of the ac field was set to be perpendicular to the 2D plane. The measurements were carried out at frequencies of 17 Hz (a), 997 Hz (b), 10 kHz (c), 100 kHz (d) and 3.2 MHz (e).
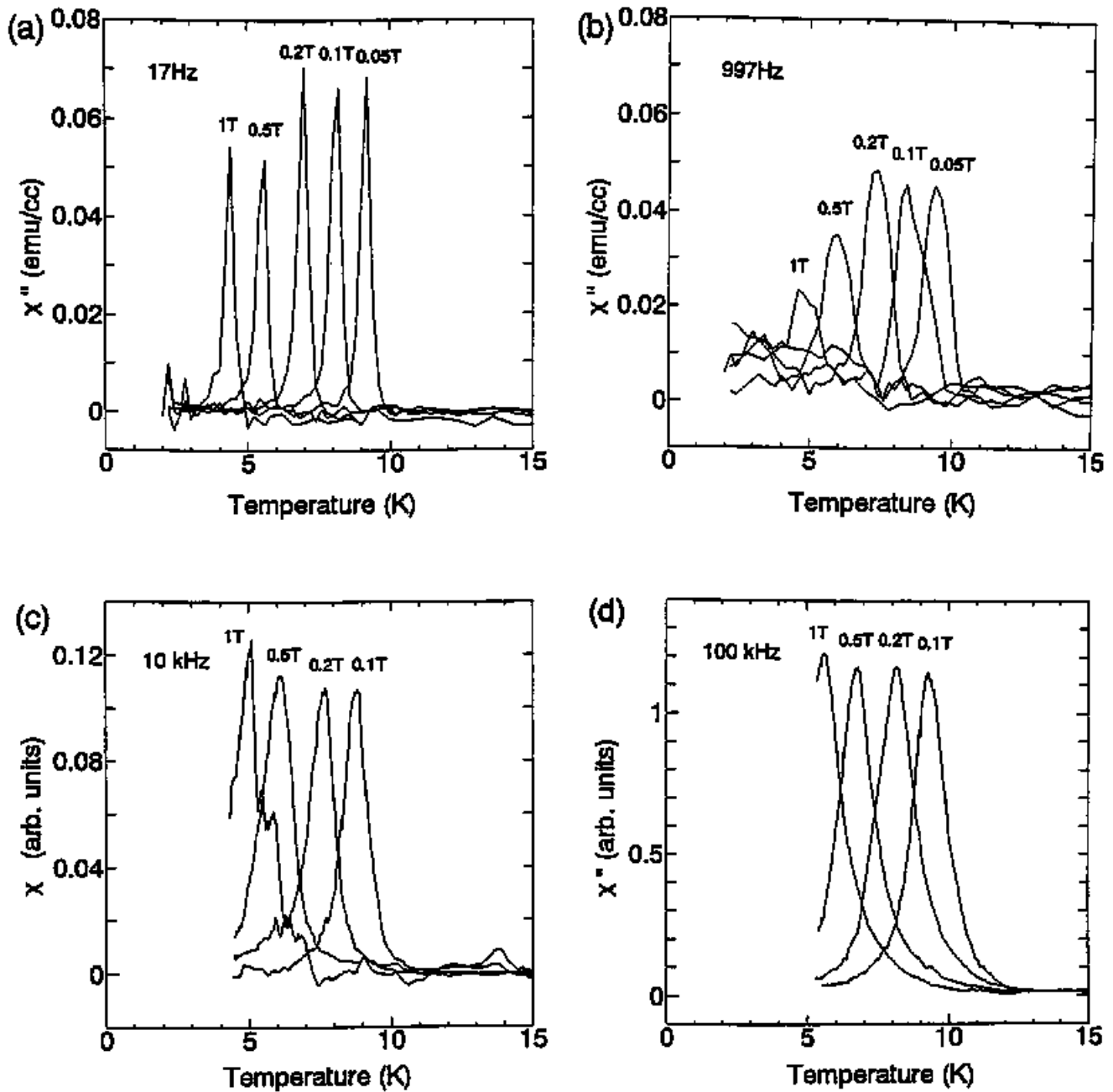
Figure 5.3: The temperature dependences of the imaginary part of the ac susceptibility for κ-(BEDT-TTF)$_2$Cu[N(CN)$_2$]Br under dc magnetic fields perpendicular to the 2D conducting plane. The direction of the ac field was set to be perpendicular to the 2D plane. The measurements were carried out at 17 Hz (a), 997 Hz (b), 10 kHz (c) and 100 kHz (d).
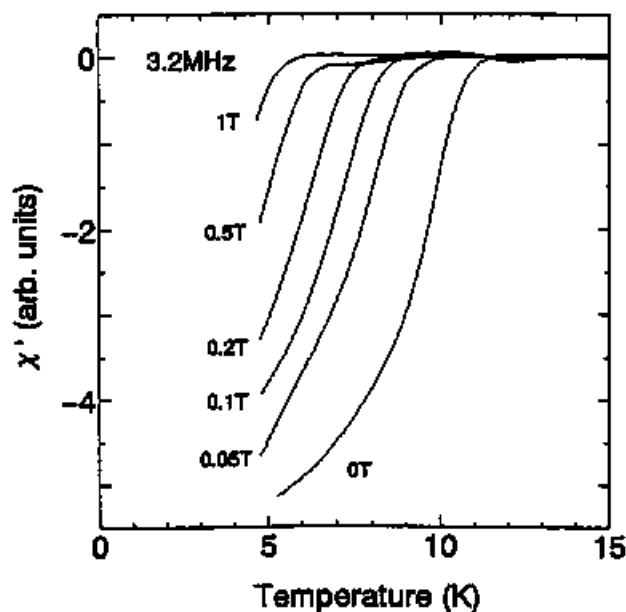
Figure 5.4: The temperature dependences of the real part of the ac susceptibility at 3.2 MHz applied parallel to the 2D plane under dc magnetic fields applied perpendicular to the 2D plane.

the transition in the real part, the imaginary part vanishes. This indicates that the superconductivity is in the reversible region with respect to the field cycling. The temperature region with nonzero imaginary part becomes wider as the frequency increases, corresponding to the behavior of transition width of the real part.

The temperature dependence of the real part of the magnetic susceptibility for 3.2±0.05 MHz ac field applied *parallel* to the 2D plane is shown in Fig. 5.4. The behavior is different from that for the ac field applied perpendicular to the 2D plane (shown in Fig. 5.2(e)). In this case, the onset of the transition shifts toward lower temperature with the increase of dc magnetic field, similarly to the cases for the ac field of lower frequency (Fig. 5.2(a~d)), although the transition is broad even at zero dc magnetic field. We could not get the result for the low frequency in this ac field direction, due to the restriction of sample configuration for the SQUID apparatus. In the intermediate frequency region, we have measured the susceptibility at 20 kHz and 100 kHz in this configuration (not shown). The behavior was found to be similar as that at 3.2 MHz, however, the signal was so small that it was hard to compare quantitatively with the data at 3.2 MHz.

The temperature dependences of the onset field of the transition for the data presented in Figs. 5.2 and 5.4 are summarized in Fig. 5.5. The onset fields decrease remarkably with decreasing frequency from 3.2 MHz to 17 Hz for the ac field applied perpendicular to the plane. In the same
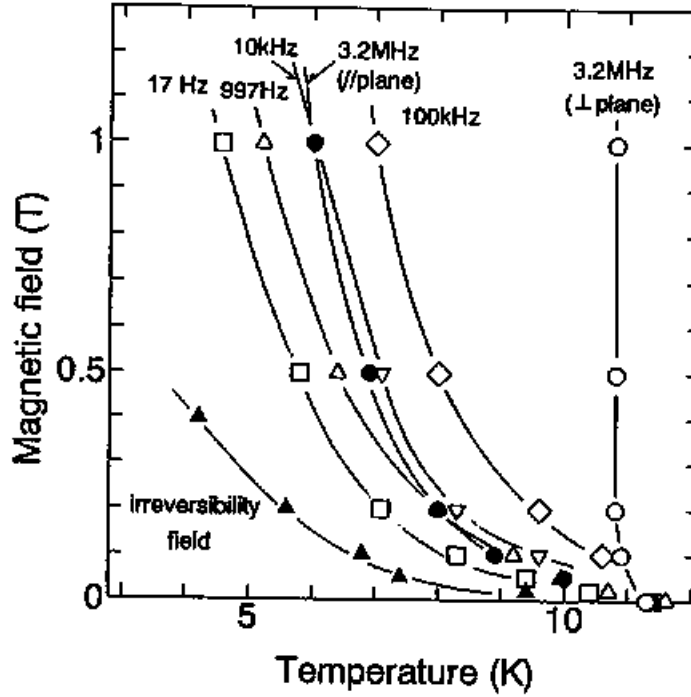
Figure 5.5: The temperature dependences of the onset of the diamagnetic susceptibility for the *ac* field applied perpendicular to the 2D plane (open marks represent the data extracted from Figs. 5.2(a), 5.2(b), 5.2(c), 5.2(d) and 5.2(e), and for the *ac* field applied parallel to the 2D plane (closed circle, extracted from Fig. 5.4). The temperature dependence of the irreversibility field is also shown in the figure (closed triangle). Note that the onset fields of the *ac* field screening stay above the irreversibility field. (Solid lines are guide for eyes.)

figure the onset fields for the *ac* field parallel to the plane (Fig. 5.4) are plotted together with the irreversibility field, measured as the merging point of the zero-field-cooled and the field-cooled *dc* magnetization. It is found that all of the onset points of the diamagnetic transition in the *ac* susceptibility are found to be higher than the *dc* irreversibility temperature T_I. This implies that the appreciable changes in the screening signal appear in the reversible region in the temperature versus magnetic-field phase diagram.

5.2.2 κ-(BEDT-TTF)$_2$Cu[N(CN)$_2$]Cl

The magnetic susceptibility data for κ-(BEDT-TTF)$_2$Cu[N(CN)$_2$]Cl at frequency of 1.9±0.1 MHz are shown in Fig. 5.6(a) and 5.6(b), for the *ac* field perpendicular (a) and parallel (b) to the 2D plane as a function of *dc* field applied perpendicular to the plane. Although the 2D structure is quite similar to κ-(BEDT-TTF)$_2$Cu[N(CN)$_2$]Br salt, κ-(BEDT-TTF)$_2$Cu[N(CN)$_2$]Cl is an insulator at ambient pressure and requires the hydrostatic pressure above 30 MPa to sta-
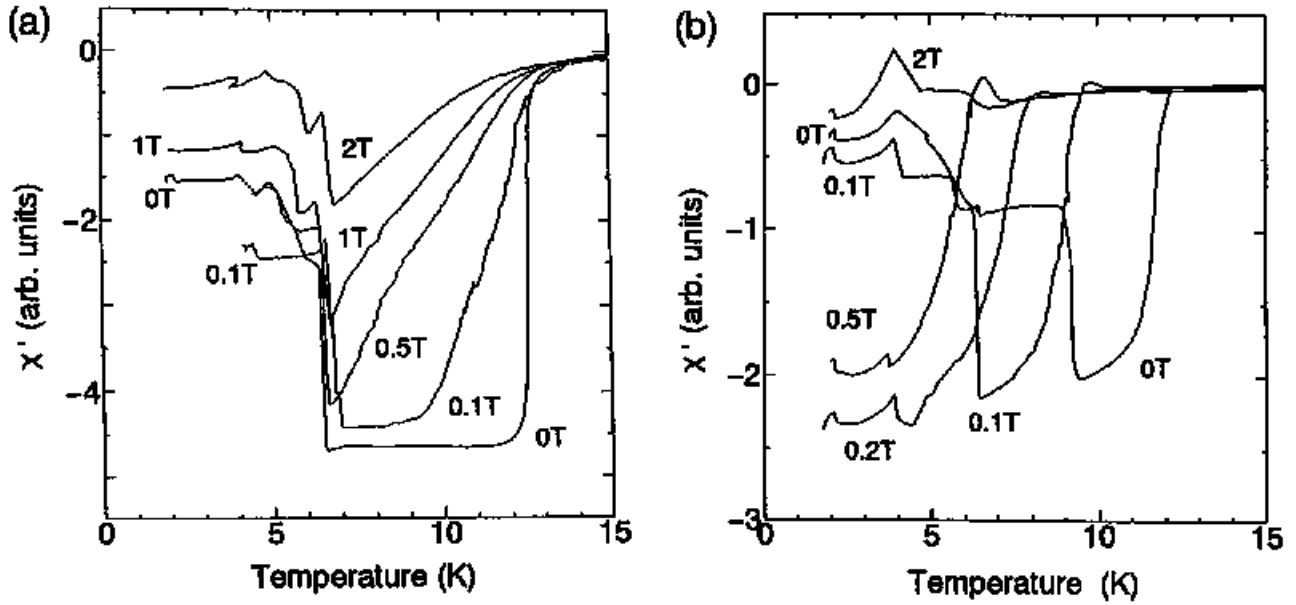
Figure 5.6: The temperature dependences of the real part of the ac susceptibility at 1.9 MHz, under dc magnetic fields applied perpendicular to the 2D plane, for the superconductivity state of κ-(BEDT-TTF)$_2$Cu[N(CN)$_2$]Cl stabilized under pressure. The ac field is applied either perpendicular (a) or parallel (b) to the 2D plane. The superconductivity is suppressed below ~6.7 K due to the emergence of non-metallic state.

bilize the superconducting state (cf. Chapter 1) [12]. For the present measurement, we applied hydrostatic pressure of 37 MPa for Fig. 5.6(a) and 55 MPa for Fig. 5.6(b) with He gas as a pressure medium. The diamagnetic signal due to the superconductivity transition is suppressed near 6.7 K, resulting in the reentrant superconductivity [12,68]. Apart from this peculiarity due to the competition between the superconductivity and the non-metallic states inherent for this material, the difference in the temperature dependence with respect to the ac field direction is similar to the case for κ-(BEDT-TTF)$_2$Cu[N(CN)$_2$]Br, shown in Fig. 5.2(e) and Fig. 5.4. That is, for the ac field perpendicular to the 2D plane, the onset temperature of the screening hardly changes while the transition is broaden with the increase of the dc magnetic field (Fig. 5.6(a)). For the ac field parallel to the 2D plane, the onset of the screening shifts toward lower temperature with the increase of the dc magnetic field (Fig. 5.6(b)). This resemblance indicates that the superconductivity transition in κ-(BEDT-TTF)$_2$Cu[N(CN)$_2$]Cl is of similar 2D nature as κ-(BEDT-TTF)$_2$Cu[N(CN)$_2$]Br. Due the restriction of the sample space in SQUID apparatus, we cannot obtain the low frequency data for the superconducting state of this salt.

5.3   Outline of the *ac* Susceptibility Theory

In order to explain the variation of the temperature (T) dependence of the magnetic susceptibility with the frequency ($\omega/2\pi$) of the *ac* field applied perpendicular to the 2D plane, in the presence of *dc* magnetic field (B) applied perpendicular to the 2D plane, we apply a linear response theory on the self-consistent fluxoid dynamics after Coffey and Clem [69,70]. This theory describes the magnetic susceptibility of superconductors by taking account of the electromagnetic dynamics of fluxoids and the skin size effects caused by quasiparticles, self-consistently. The theory has been developed for an isotropic material, but we consider that it is applicable for 2D superconductor provided that both of the *ac* and *dc* magnetic fields are perpendicular to the 2D plane, since the related screening currents can flow within the isotropic conducting plane. The outline of the theory is briefly presented below.

First we assume a semi-infinite isotropic superconductor, occupying the region $x > 0$. Both *ac* and *dc* fields applied parallel to the z axis. We start with an equation of motion of a fluxoid, including the flux flow and the flux creep effects, given as,

$$\eta \dot{u}(x,t) + \kappa_p u(x,t) + F(t) = J(x,t) \times \phi_0 \hat{z} \, , \qquad (5.1)$$

where $u(x,t)$ is the displacement of the fluxoid from its equilibrium pinning site. η is a viscous drag coefficient and κ_p is a restoring force constant (Labusch parameter). $F(t)$ is a random Langevin force to describe the thermally activated depinning from the pinning site (flux creep). The right hand side denotes the Lorentz force exerted on the fluxoid. ϕ_0 is a flux quantum and $\hat{z}$ is a unit vector in the z direction. Here we apply the two-fluid model to take account of the normal skin depth effect; the current $J(x,t)$ includes not only supercurrent but also quasiparticle current. By the motion of the fluxoids, the additional magnetic field $\delta b(x,t)$ is generated as,

$$\delta b(x,t) = \sum_j \frac{\partial b(x,x_j)}{\partial x_j} u(x_j,t) \, ,$$

where $b(x,x_j)$ is a local magnetic field at position x generated by a fluxoid locates at x_j. $u(x_j,t)$ is the displacement of the j-th fluxoid which assumed to be,

$$u(x_j,t) = \hat{x} u_0 e^{-x_j/\tilde{\lambda}} e^{-i\omega t} \, ,$$

where $\tilde{\lambda}$ is a complex effective penetration depth, from which the *ac* susceptibility is calculated. u_0 is proportional to the amplitude of the applied *ac* field and $\hat{x}$ is a unit vector in the x direction.

Simultaneously we adopt the modified diffusive London equation for external *dc* field B,

$$\nabla^2 B = \frac{\mu_0}{\rho_n(T)/(1-f)}\dot{B} + \frac{1}{\lambda(B,T)}(B - \phi_0 n\hat{z}). \tag{5.2}$$

The first term in the right hand side arises from the quasiparticle current. f and $\rho_n(T)$ denote the superfluid fraction in the two-fluid model and the normal resistivity, respectively. The second term is the supercurrent contribution. $\lambda(B,T)$ is the London penetration depth. The average fluxoid density n is calculated by integrating the continuity equation between alternating field $\delta b(x,t)$ and the external *ac* field at the surface of the superconductor.

By solving above differential equations, we get $\tilde{\lambda}$ as,

$$\tilde{\lambda} = \sqrt{\frac{\lambda(B,T)^2 + i/2\tilde{\delta}_{vc}^2}{1 - 2i\lambda(B,T)^2/\delta_{nf}^2}}. \tag{5.3}$$

We note that the amplitude of the *ac* field does not come into this formula in the linear response regime. The term $\tilde{\delta}_{vc}^2$ represents the correction to the London penetration depth arises from the fluxoid motion, and is proportional to a fluxoid mobility $\tilde{\mu}_v$ as,

$$\tilde{\delta}_{vc}^2 = \frac{2B\phi_0}{\mu_0\omega}\tilde{\mu}_v \,, \tag{5.4}$$

where $\tilde{\mu}_v$ is represented as,

$$\tilde{\mu}_v = \frac{1}{\eta}\left[1 + \left[-\frac{i\omega\eta}{\alpha\kappa_p(T)} + \frac{1}{I_0^2(\nu) - 1}\right]^{-1}\right]^{-1} \tag{5.5}$$

The parameter $\nu = U(B,T)/2k_{\mathrm{B}}T$ represents a thermally activated fluxoid depinning, analogous to a particle undergoing Brownian motion at the bottom of a local potential well in a periodic potential $U(u) = U(B,T)/2[1 - \cos(2\pi u/a_p)]$. a_p is related to κ_p as $\kappa_p = (U(B,T)/2L)(2\pi/a_p)^2$. α is the ratio $\alpha = I_1(\nu)/I_0(\nu)$, where I_n denotes the n-th modified Bessel function. The term δ_{nf}^2 represents the skin depth effect due to quasiparticle and is given by,

$$\delta_{nf}^2 = \frac{\delta_n^2}{1-f} \,, \tag{5.6}$$

where $\delta_n^2 = 2\rho_n(T)/(\mu_0\omega)$ is the normal skin depth.

Using $\tilde{\lambda}$ obtained for semi-infinite superconductor, the complex susceptibility $\tilde{\chi}$ is analytically calculated for simple sample geometries by taking account of appropriate boundary condition [70]. In the case of a infinite prism of $w \times w$ square cross section, $\tilde{\chi}$ is written as,

$$\tilde{\chi} = \chi' + i\chi'' = \frac{2\tilde{\lambda}}{w}\tanh\left[\frac{w}{2\tilde{\lambda}}\right] + \frac{16\tilde{\lambda}}{\pi^2 w}\sum_{n=0}^{\infty}\frac{\tanh(q_n w/2)}{(2n+1)^2(k_n^2\tilde{\lambda}^2+1)^{3/2}} - 1 \,, \tag{5.7}$$

where $k_n = (2n+1)\pi/w$ and $q_n = \sqrt{\tilde{\lambda}^{-2} + k_n^2}$. Here χ' and χ'' denotes the real and imaginary part of $\tilde{\chi}$. In the calculation, the summation up to index $n = 100$ is enough to reach convergence.

Then we get the temperature and dc magnetic field dependences of the parameters based on the two-fluid model by taking account of the quasiparticle excitation via pair-breaking process in the mean-field approximation, as follows,

$$\lambda(B,T) = \frac{\lambda(0)}{\sqrt{(1-t^4)(1-B/B_{C2}(T))}} \,, \tag{5.8}$$

$$\kappa_p = \kappa_{p0}(1-t^2)^2 \,, \tag{5.9}$$

$$f = (1-t^4)[1-B/B_{C2}(T)] \,, \tag{5.10}$$

$$B_{C2}(T) = B_{C2}(0)(1-t^2)/(1+t^2) \,, \tag{5.11}$$

where t denotes the reduced temperature scaled with the superconducting transition temperature at zero magnetic field T_{C0}, as $t = T/T_{C0}$. Here we assume the temperature dependence of the London penetration depth obeys Gorter-Casimir law as given by Eq. (5.8), laying aside the arguments related to the symmetry of the superconducting pairing [71,72]. By employing the Bardeen-Stephan expression, the viscous drag coefficient η is given by [50],

$$\eta = \frac{\phi_0 B_{C2}(T)}{\rho_n(T)}. \tag{5.12}$$

Based on the thermally assisted flux flow model, the pinning potential $U(B,T)$ is deduced as [52,53],

$$U(B,T) = U_0(1-t)^{3/2}/B. \tag{5.13}$$

5.4 Discussion

In this section we first analyze the frequency dependence of the ac susceptibility for κ-(BEDT-TTF)$_2$Cu[N(CN)$_2$]Br, shown in Figs. 5.2(a), 5.2(b), 5.2(c), 5.2(d) and 5.2(e), based on the formulae given in the previous section. Then we interpret the anisotropy with respect to the ac field direction at 3.2 MHz, represented by Fig. 5.2(e) and Fig. 5.4.

5.4.1 Calculated susceptibility for the ac field perpendicular to the plane

By applying the self-consistent electromagnetic theory represented in the previous section, we calculate the ac susceptibility, by varying the physical parameters to reproduce the experimental results given in Figs. 5.2(a), 5.2(b), 5.2(c), 5.2(d) and 5.2(e). For this purpose we examine the parameter values one by one, referring available experimental data. We set the superconducting transition temperature at the zero external magnetic field T_{C0} to be 11.5 K. The London penetration depth in the direction perpendicular to the 2D plane at absolute zero temperature, $\lambda(0)$, is given as 800 nm from the μSR measurement [73] and as 780 nm from the dc magnetization [72]. The upper critical field at absolute zero temperature is given as $B_{C2}(0) = \phi_0/(2\pi\xi_\parallel(0)^2)$ in the mean-field treatment. We get 60±20 T by using the intraplane coherence length $\xi_\parallel(0)$=2.3±0.4 nm deduced from the analysis of dc magnetization described in Chapter 3. We remark that this B_{C2} is a theoretical entity and is not necessarily related to the experimental upper critical field, which is hard to be determined due to the thermal fluctuation. As the normal resistivity $\rho_n(T)$, which is necessary to calculate the normal skin depth, we used the quadratic functional fit of the in-plane resistivity in a magnetic field of 10 T, applied perpendicular to the crystal plane, as shown in Fig. 4.3(a) in Chapter 4. However, due to the limitations in the size and shape of the sample and also the magnetoresistance effect in the normal state, we have to allow uncertainty reaching factor of 3 for $\rho_n(T)$. On the calculation we searched appropriate $\rho_n(T)$ by multiplying a factor ranging 0.3~3 onto the evaluated $\rho_n(T)$ value. Concerning the pinning potential U_0, we find the value of 7±1meV·T by the way shown in Chapter 4. We set the Labusch parameter κ_{p0} at absolute zero temperature to be 1~10 N/m^2 in order to reproduce the observed offset of the ac susceptibility appearing in the low temperature region. This parameter range is larger than the value for κ-(BEDT-TTF)$_2$Cu(NCS)$_2$ as 0.07 N/m^2 evaluated from the magnetic field dependence of the effective penetration depth in the low temperature region [74]. We remark that these

Labusch parameters evaluated for organic superconductor are 4~5 order smaller than that for the high-T_c cuprate superconductors. Finally, we approximate the sample shape with a square plate of size $w=1$ mm enabling to use the analytical formulae. We do not take into account the demagnetization factor associated with the finite thickness of the sample. This is permitted, since we evaluate not the absolute value but the relative variations of the susceptibility. The calculated result is not affected in the linear response regime.

The calculated susceptibilities so as to reproduce the experimental data at five different frequencies, 17 Hz, 997 Hz, 10 kHz, 100 kHz and 3.2 MHz, are shown in Figs. 5.7(a), 5.7(b), 5.7(c), 5.7(d) and 5.7(e), respectively. The used parameters are $\lambda(0)=800$ nm, $T_{C0}=11.5$ K, $B_{C2}(0)=60$ T, $U_0=7$ meV·T and $\kappa_{p0}=2$ N/m^2 The used normal resistivity is $\rho_n(T) = 0.014T^2 - 0.04T + 5.8$ (mΩcm), which is multiplied by 1.5 onto the evaluated $\rho_n(T)$ in order to reproduce the curvature of the observed transition curves at 3.2 MHz. We find that the calculated χ' reproduces the observed specific frequency dependence rather well. The corresponding imaginary part χ'' at 17 Hz, 997 Hz, 10 kHz and 100 kHz are shown in Figs. 5.8(a), 5.8(b), 5.8(c) and 5.8(d), respectively. The calculated reproduces the observed at 17 Hz, 10 kHz and 100 kHz, while the calculated at 997 Hz is sharper than the observed.

In order to understand the origin of the frequency dependence, the temperature dependences of the characteristic lengths are illustrated in Figs. 5.9(a), 5.9(b), 5.9(c), 5.9(d) and 5.9(e); the real part of the effective complex penetration depth $\tilde\lambda$, Re$[\tilde\lambda]$, and three specific contributions to this, i.e., the London penetration depth $\lambda(B,T)$, the real part of the fluxoid penetration depth $\tilde\delta_{vc}$, and the skin depth δ_{nf} due to the quasiparticle motion. The calculated results are given for five frequencies, 17 Hz (a), 997 Hz (b), 10 kHz (c), 100 kHz (d) and 3.2 MHz (e). Here we show the calculated at the dc magnetic field of 0.2 T as a representative: the specific relations between the characteristic lengths are common for all cases of the dc magnetic fields adopted in Fig. 5.7. It is found that the total complex penetration depth $\tilde\lambda$ is dominated by the fluxoid penetration depth $\tilde\delta_{vc}$, determined by the fluxoid flow and creep effects. The relation between the characteristic lengths/depth and the half of the sample width of $w/2=0.5$ mm characterizes the temperature dependence of the susceptibility at each frequency. For example, in the case of 17 Hz, Re$[\tilde\lambda]$ crosses 0.5 mm line at 7.2 K. Above this temperature, Re$[\tilde\lambda]$ is longer than the sample size, so that the ac field prevails all over the sample, i.e., the diamagnetic screening signal hardly appears. Below
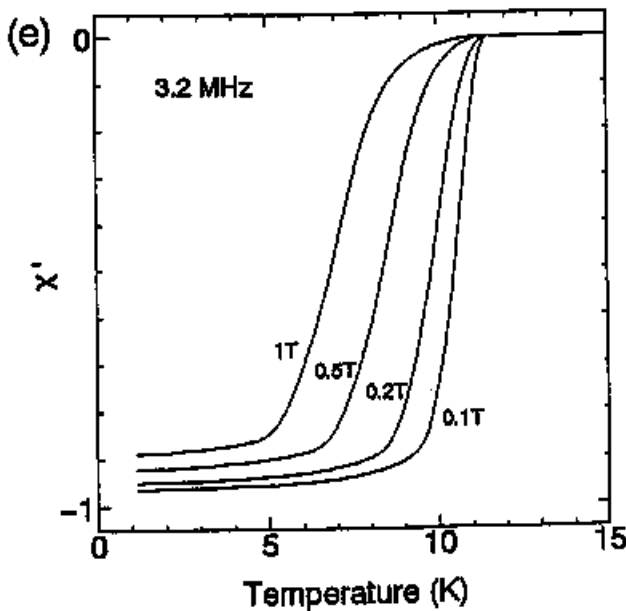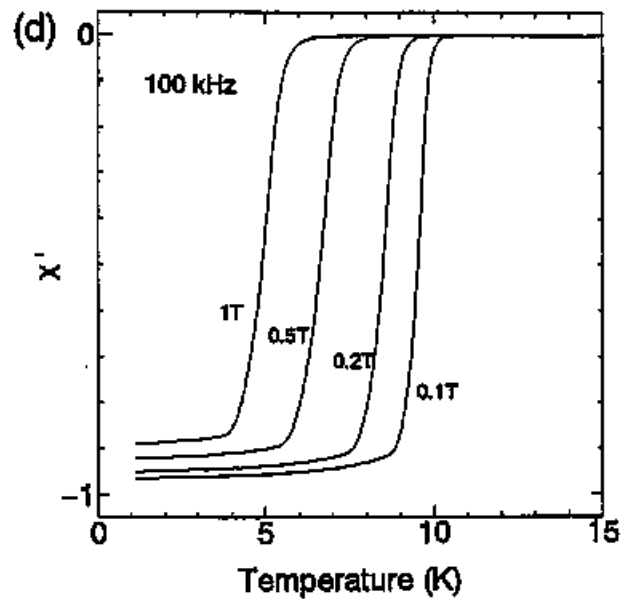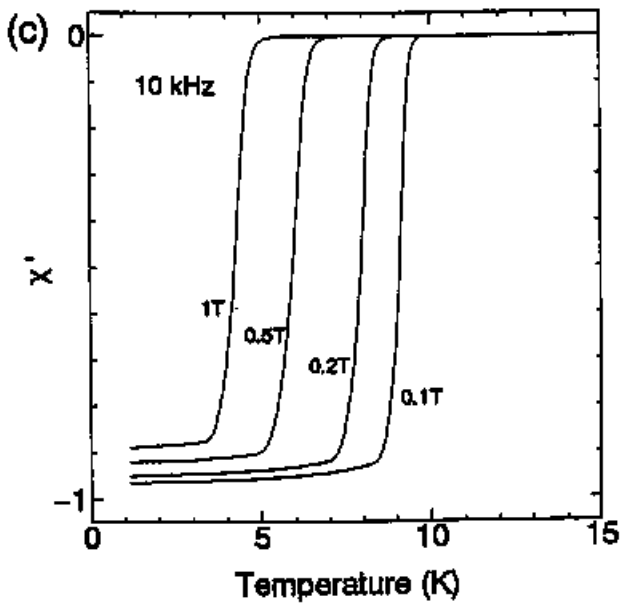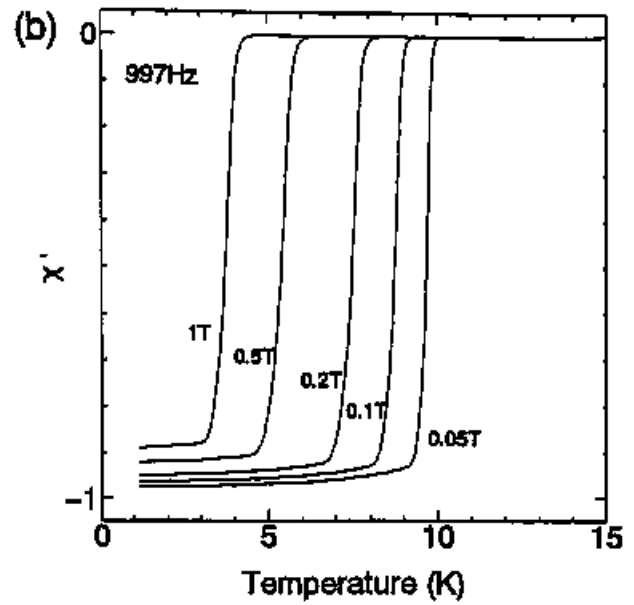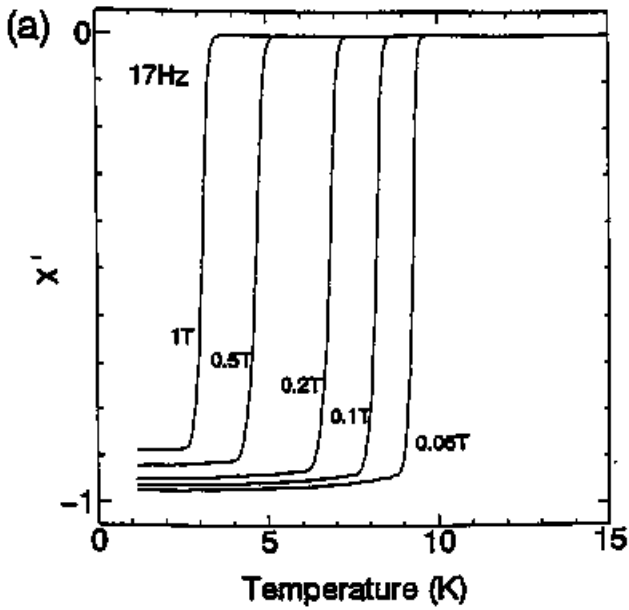
Figure 5.7: Calculated real part of the *ac* susceptibility in the mixed state by the self-consistent fluxoid dynamics theory corresponding to 17 Hz (a), 997 Hz (b), 10 kHz (c), 100 kHz (d) and 3.2 MHz (e). Concerning used material parameters, see the text.

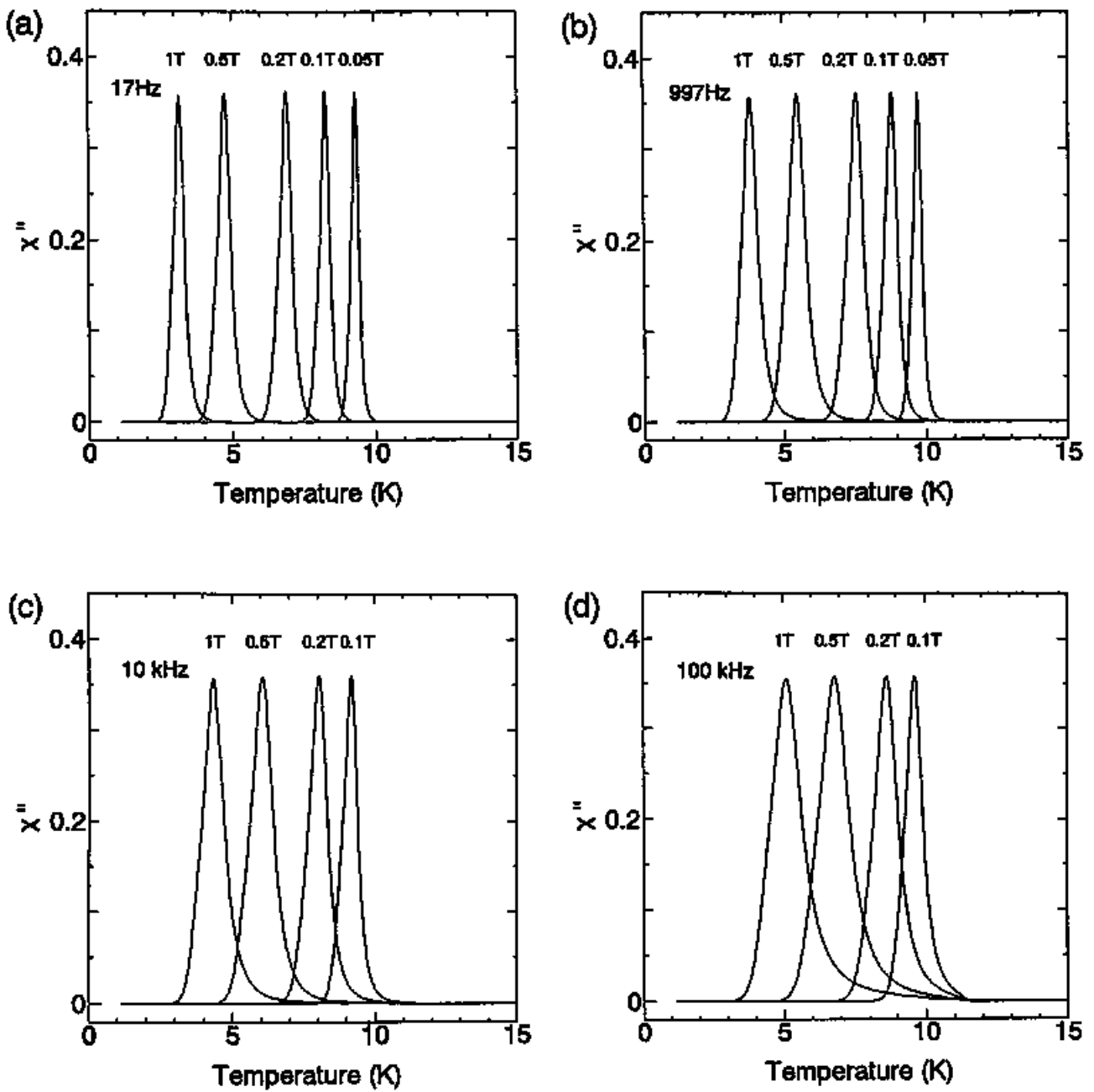Figure 5.8: Calculated imaginary part of the ac susceptibility in the mixed state by the self-consistent fluxoid dynamics theory corresponding to 17 Hz (a), 997 Hz (b), 10 kHz (c) and 100 kHz (d). Concerning used material parameters, see the text.
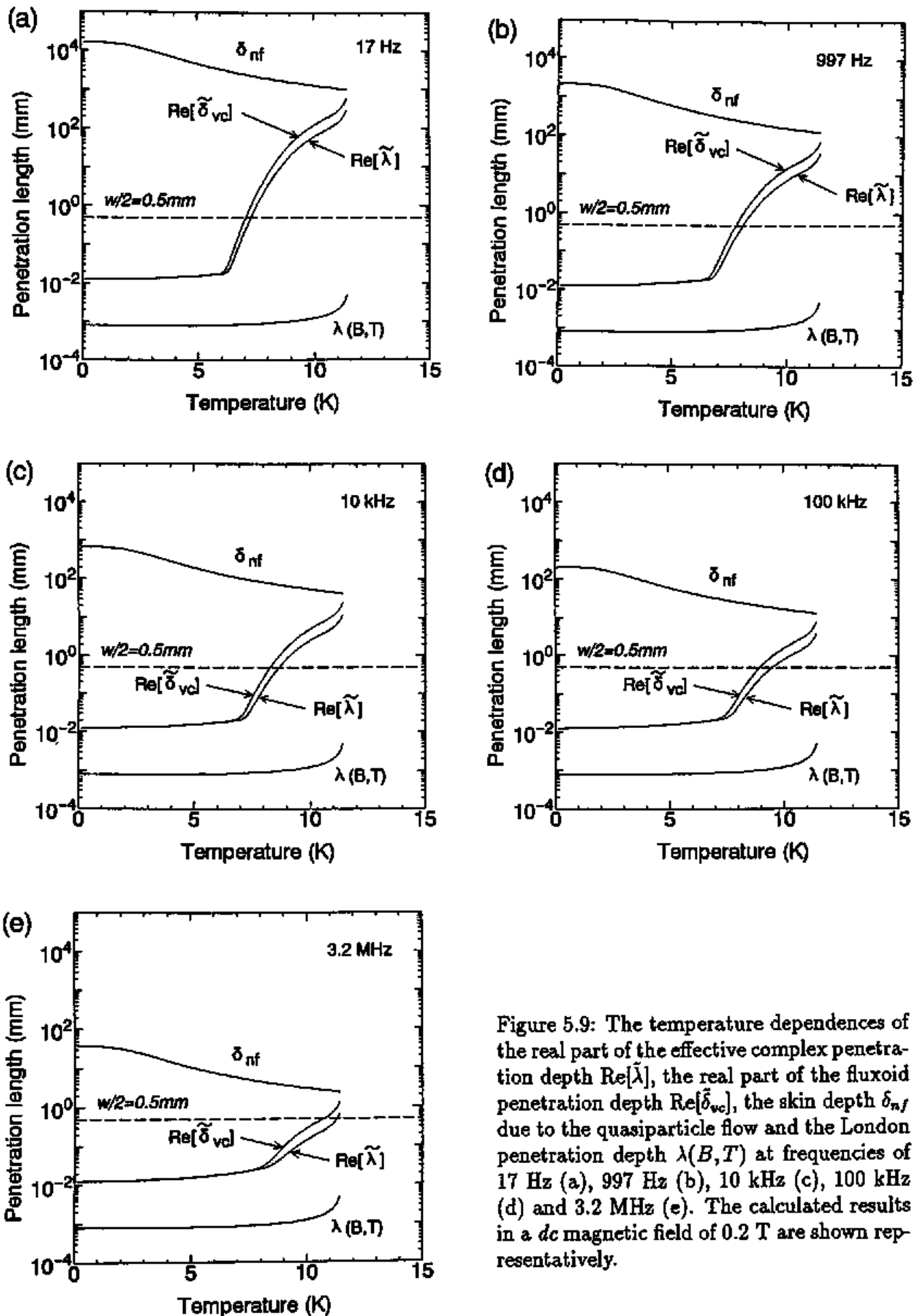
Figure 5.9: The temperature dependences of the real part of the effective complex penetration depth $\text{Re}[\tilde{\lambda}]$, the real part of the fluxoid penetration depth $\text{Re}[\tilde{\delta}_{vc}]$, the skin depth δ_{nf} due to the quasiparticle flow and the London penetration depth $\lambda(B,T)$ at frequencies of 17 Hz (a), 997 Hz (b), 10 kHz (c), 100 kHz (d) and 3.2 MHz (e). The calculated results in a *dc* magnetic field of 0.2 T are shown representatively.

this temperature the penetration depth becomes shorter than the sample size, so that there exists a portion screened from the ac field. These crossover points agree with the point of the steepest diamagnetic transition under dc field of 0.2 T calculated as Figs. 5.7(a~d). On the other hand, at 3.2 MHz, $\text{Re}[\tilde{\lambda}]$ is shorter than the sample size in almost all of the temperature region, except that very close to T_c. Thus the ac field is screened almost all over the temperature region. In this case the quasiparticle skin depth δ_{nf} becomes short and comparable to the sample size. At frequency less than 1 kHz, we can neglect the contribution of the skin depth which is far longer that the sample size. However, at 3.2 MHz the skin depth contribution becomes important for the screening. In fact, the calculated susceptibility at 3.2 MHz is sensitive to the $\rho_n(T)$ value. The London penetration depth $\lambda(B, T)$ is frequency-independent and much shorter than the sample size.

The frequency dependence of the ac susceptibility is explained fairly well with the electrodynamic theory of the fluxoid dynamics and the quasiparticle skin size effects, although we cannot dismiss the adopted approximation, such as the sample geometry and the mean-field treatment. We give several remarks below in order to understand the observed more definitely.

(1) In the low frequency region, the calculated real and imaginary parts of the susceptibility are improved to fit the observed, if we use smaller κ_p and larger U_0 values in the case of high dc field. With smaller κ_p, the offset level of χ' in the low temperature is raised upward, whereas with larger U_0 the onset temperature of the transition shifts to higher temperature. This implies that the collective creep effect, which is not taken into account in the present theory, becomes important in the high fluxoid density region.

(2) From the comparison of the effective penetration depths, we find that the diamagnetic transition onset temperature of ac susceptibility in the low frequency region (~1 kHz) should depend on the sample size w.

(3) At the rf frequency, the calculated are found to be sensitive to the normal resistivity $\rho_n(T)$ through the normal skin depth. In the present study we adopted the quadratic variation of the resistivity in the high dc field, but by using more precise temperature dependence of $\rho_n(T)$ the fitting will be improved. In the case of κ-(BEDT-TTF)$_2$Cu[N(CN)$_2$]Cl, as shown in Fig. 5.6(a), the broadening nature of the diamagnetic transition looks slightly different from that of κ-(BEDT-TTF)$_2$Cu[N(CN)$_2$]Br. This is partly ascribed to the difference in $\rho_n(T)$, since in this case the

normal resistivity is reduced by the application of the hydrostatic pressure.

(4) We cannot neglect the effect of sample inhomogeneity, which is found on the dullness in the diamagnetic transition even in the absence of the *dc* magnetic field, for the better reproduction of the observed. Such inhomogeneiety becomes more effective at higher frequency region where the normal skin depth effect becomes dominant.

(5) We approximated the sample shape with a infinite prism of the square cross section. In the case of a plate with finite thickness, the screened *ac* magnetic field which has to go round the sample plane may contain a parallel component of the *ac* field.

(6) The 2D conducting plane, which we have been assumed to be isotropic, is not of complete isotropy, as indicated by the calculated Fermi surface shown as Fig. 1.5(b).

A part of the discrepancy between the calculated and the observed may be ascribed to (4), (5) and (6). However, the considerable success of the fitting for the frequency variation covering 5 orders implies that the dominant mechanism has been seized by the present analysis.

5.4.2 Susceptibility for the *ac* field parallel to the plane

In the case of the *rf* field applied parallel to the 2D plane, as shown in Fig. 5.4 for κ-(BEDT-TTF)$_2$Cu[N(CN)$_2$]Br and Fig. 5.6(b) for κ-(BEDT-TTF)$_2$Cu[N(CN)$_2$]Cl, the diamagnetic signal shows broad transition even in the absence of the *dc* magnetic field. This is due to the long London penetration depth parallel to the 2D plane reaching 0.2 mm for κ-(BEDT-TTF)$_2$Cu[N(CN)$_2$]Br [75], comparable to the sample thickness. The temperature dependence of the penetration depth broadens the diamagnetic transition in the susceptibility for *ac* field parallel to the 2D plane.

To discuss the *dc* field dependence of the *ac* susceptibility in this configuration, the analytical theory used in the previous section cannot be applied. We must take into account the effect of the interplane conduction, since the screening current flows *penetrating* the 2D superconducting plane. Here we point out that the normal skin depth effect is not so effective as the case for *ac* field applied perpendicular to the 2D plane. That is, the skin depth for this current direction is much larger compared to the sample size, due to the large resistivity in the interplane direction. Thus the behavior of the *ac* screening signal is considered similar to that at lower frequency, as shown in Figs. 5.2(a~d), although this has not been confirmed by experiment due to the restriction of the apparatus.

In order to explain the shift in the onset temperature of the screening, we take account of the interplane decoupling effect. In the case of 2D superconductor, possessing interplane coherence length shorter than the interplane spacing, the interplane coupling can be modeled by the Josephson mechanism [63]. The phase coherence for the interplane direction vanishes even at a temperature well below T_{c0} under the magnetic field perpendicular to the 2D plane, due to the phase fluctuation across the 2D layers [76]. The decoupling temperature T_d almost coincides with the temperature where the fluxoid lines decompose into pancake fluxoids confined into each 2D plane, and is given as,

$$T_d = A/(1 + B/B_1) , \qquad (5.14)$$

where A and B_1 are constants [77]. For $T > T_d$ each superconducting plane behaves independently and the coherent supercurrent is suppressed in the interplane direction. As a result, the ac field parallel to the 2D plane is hardly screened in the decoupled state. The onset temperature of the ac field expulsion corresponds to the temperature where the pancake fluxoids in the individual plane unite with each other to form one fluxoid line.

This kind of the interplane decoupling effect is reported by de la Cruz et $al.$ for the 2D cuprate superconductor $Bi_2Sr_2CaCu_2O_8$ and $YBa_2Cu_3O_7$[78]. In the case of $Bi_2Sr_2CaCu_2O_8$, the susceptibility for the ac field parallel to the 2D plane in the presence of dc magnetic field shows two peaks in the imaginary part and the peak in the lower temperature side locates below the dc irreversibility temperature T_I. They claim that this extra peak corresponds to the suppression of the interplane screening current, i.e., the fluxoid decoupling at the peak temperature, which is lower than T_I. On the other hand, for the less 2D superconductor $YBa_2Cu_3O_7$, the resistivity measurement using the flux-transformer geometry showed the fluxoid decoupling in the resistive state, and therefore T_d becomes higher than T_I [79].

In the case of κ-(BEDT-TTF)$_2$Cu[N(CN)$_2$]Br, the onset temperature of the screening for the ac field parallel to the 2D plane locates higher than the dc irreversibility temperature (Fig. 5.5) like the case for $YBa_2Cu_3O_7$. This implies that the region in the temperature versus magnetic-field phase diagram above the irreversibility line is divided into two region. In the high temperature side above the phase boundary, the fluxoids are decoupled into the pancake fluxoids, while below the boundary they are connected to form the fluxoid lines penetrating the 2D superconducting

planes. The phase boundary line, above which the interplane screening current is suppressed, seems to be frequency-independent. However, the behavior of susceptibility for the parallel ac field will be different between the high and the low frequency regimes. At 3.2 MHz, the in-plane screening current is flowing almost all temperature region below T_c. The ac field applied parallel to the 2D plane is screened when the interplane screening current flows as well as the in-plane one, below the phase boundary line. On the other hand at low frequency region, $e.g.$, below 1 kHz, the onset temperature of the screening for the ac field applied *perpendicular* to the 2D plane becomes lower than the boundary line. In this case an intermediate region exists where the interplane screening current starts to flow but the in-plane screening current is still suppressed. In this region the parallel ac field is not screened due to the lack of in-plane screening current. The screening for the parallel ac field will be achieved below the onset point of the perpendicular ac field screening. Therefore, in this frequency region, the onset temperatures of the screening for the ac field applied perpendicular and parallel to the 2D plane are expected to coincide with each other.

5.5   Concluding Remarkes of Chapter 5

The magnetic susceptibility measurements have been adopted to characterize the superconductivity transition characteristics. Particularly, the rf susceptibility provides a highly sensitive means of probing fluxoid dynamics in type II superconductors, which can be carried out in a restricted space $e.g.$ in a pressure cell as in the case of κ-(BEDT-TTF)$_2$Cu[N(CN)$_2$]Cl. However, the experimental results look rather complicated in particular for 2D superconductor in the presence of the external dc magnetic fields.

In this chapter we have shown that the frequency-dependent behavior of the susceptibility for the ac field applied perpendicular to the 2D plane can be fairly well understood based on the self-consistent electromagnetic treatment of the fluxoid dynamics including flux flow, flux creep and normal skin depth effects. The fluxoid motion plays important role on the ac susceptibility and the normal skin size effect due to the quasiparticle motion cannot be neglected at high frequency. The interplane decoupling effect takes a dominant role for the ac field parallel to the plane.

Chapter 6

Summary

The effect of two-dimensionality onto the superconductivity transition characteristics has been elucidated through the studies on the thermal fluctuation and the fluxoid dynamics effects, appearing in the magnetic and resistive behaviors for the κ-type BEDT-TTF organic superconductors.

In Chapter 3, we have treated the diamagnetic superconductivity transition through dc magnetization measurements in the presence of the magnetic field, taking account of the thermal fluctuation in terms of the renormalized theory. Through the analysis we deduced the superconductivity coherence length for organic superconductors on the reliable quantitative basis for the first time. The interplane one is found to be shorter than the interplane spacing. This asserts that the superconductivity state is of 2D nature which is appropriately treated with the model of Josephson-coupled two-dimensional superconductor (Lawrence-Doniach model). By the scaling analysis, we found that κ-(BEDT-TTF)$_2$Cu(NCS)$_2$ is more 2D than κ-(BEDT-TTF)$_2$Cu[N(CN)$_2$]Br, in agreement with the difference in the resistivity anisotropy.

In Chapter 4, we have dealt with the resistive transition. For the transport properties in the presence of magnetic field, the effect of the pinned fluxoid cannot be neglected in addition to the thermal fluctuation. The thermally assisted fluxoid flow mechanism plays more dominant role for the the resistive transition under magnetic field, than the superconductivity fluctuation. In the case of κ-(BEDT-TTF)$_2$Cu(NCS)$_2$, the weak-coupling between 2D superconducting layers influences the interplane transition properties through the quasiparticle current. Since the weak-coupling effects at some defects or stacking faults will also affect the transition characteristics in the case of inferior samples, comprehensive studies with the characterization on the sample crystalinity are needed to quote the intrinsic behavior of resistive transition.

In Chapter 5, the dynamics of the fluxoids are investigated through the ac susceptibility under dc

magnetic field for κ-(BEDT-TTF)$_2$Cu[N(CN)$_2$]Br. The frequency dependence of the susceptibility for the ac field applied perpendicular to the 2D plane is well understood by the self-consistent electromagnetic theory of fluxoid dynamics based on the mean-field approximation by paying care on its applicability. We have shown also that the direction dependence of the ac field with respect to the 2D plane onto the susceptibility behavior can be explained in terms of the interplane decoupling of the fluxoid into 2D pancake vortices.

In this thesis, the two different important aspects, the thermal fluctuation and the fluxoid dynamics, have been revealed as the specific characteristics of the κ-type BEDT-TTF layered organic superconductors under magnetic fields. Since the result obtained here is considered to be universal to the layered superconductors, the fruit will serve to put forward the general understanding of the 2D superconductors, including high-T_c cuprate superconductors.

Acknowledgements

References

[1] D. Jerome, A. Mazaud, M. Ribault, K. Bechgaard: J. Physique Lett. 41 (1980) L95.

[2] S.S.P Parkin, E.M. Engler, R.R. Schumaker, R. Laiger, V.Y. Lee, J.C. Scott and R.L. Greene: Phys. Rev. Lett. 50 (1983) 270.

[3] E.B. Yagubskii, I.F. Shchegolev, V.N. Laukhin, P.A. Kononovich, M.V. Kartsovnik, A.V Zvarykina and L.I. Buravov: JETP Lett. 39 (1984) 12.

[4] V.N. Laukhin, E.E. Kostyuchenko, Yu.V. Sushko, I.F. Shchegolev and E.B. Yagubskii: JETP Lett. 41 (1985) 81.

[5] K. Murata, M. Tokumoto, H. Anzai, H. Bando, G. Saito, K. Kajimura and T. Ishiguro: J. Phys. Soc. Jpn. 54 (1985) 2084.

[6] H. Urayama, H. Yamochi, G. Saito, K. Nozawa, T. Sugano, M. Kinoshita, S. Sato, K. Oshima, A. Kawamoto and J. Tanaka: Chem. Lett. (1988) 55.

[7] A.M. Kini, U. Geiser, H.H. Wang, K.D. Carlson, J.M. Williams, W.K. Kwok, K.G. Vandervoort, J.E. Thompson, D.L. Stupka, D. Jung and M.-H. Whangbo: Inorg. Chem. 29 (1990) 2555.

[8] J.M. Williams, A.M. Kini, H.H. Wang, K.D. Carlson, U. Geiser, L.K. Montgomery, G.J. Pyrka, D.M. Watkins, J.M. Kommers, S.J. Boryschuk, A.V Strieby Crouch, W.K. Kwok, J.E. Schirber, D.L. Overmyer, D. Jung and M.-H. Whangbo: Inorg. Chem. 29 (1990) 3272.

[9] U. Welp, S. Flesher, W.K. Kwok, G.W Crabtree, K.D. Carlson, H.H. Wang, U. Geiser, J.M. Williams and V.M. Hitsman: Phys. Rev. Lett. 69 (1992) 840.

[10] K. Miyagawa, A. Kawamoto, Y. Nakazawa and K. Kanoda: Synth. Metals, 70 (1995) 969.

[11] H. Ito, M. Kubota, Y.V. Sushko, N. Kojima, G. Saito and T. Ishiguro: Synth. Metals, 70 (1995) 925.

[12] Yu.V Sushko, H. Ito, T. Ishiguro, S. Horiuchi and G. Saito: Solid State Commun. 87 (1993) 997.

[13] Yu.V Sushko, H. Ito, T. Ishiguro, S. Horiuchi and G. Saito: J. Phys. Soc. Jpn. 62 (1993) 3372.

[14] For reviews; G. Saito, H. Yamochi, T. Nakamura, T. Komatsu, T. Ishiguro, Y. Nogami, H. Ito, H. Mori, K. Oshima, M. Nakashima, S. Uchida, H. Takagi, S. Kagoshima and T. Osada: Synth. Metals 41-43 (1991) 1993.

[15] T. Komatsu, T. Nakamura, N. Matsukawa, H. Yamochi, G. Saito, H. Ito, T. Ishiguro, M. Kusunoki and K. Sakaguchi: Solid State Commun. 80 (1991) 843.

[16] H. Urayama, H. Yamochi, G. Saito, S. Sato, A. Kawamoto, J. Tanaka, T. Mori, Y. Maruyama and H. Inokuchi: Chem. Lett. (1988) 463.

[17] H. Yamochi, T. Nakamura, T. Komatsu, N. Matsukawa, T. Inoue, G. Saito, T. Mori, M. Kusunoki and K. Sakaguchi: Solid State Commun. 82 (1992) 101.

[18] K. Nozawa, T. Sugano, H. Urayama, H. Yamochi, G. Saito and M.Kinoshita: Chem. Lett. (1988) 617.

[19] H.H. Wang, L.K. Montgomery, A.M. Kini, K.D. Carlson, M.A. Beno, U. Geiser, C.S. Cariss, J.M. Williams and E.L. Venturini: Physica C 156 (1988) 173.

[20] N. Toyota, T. Sasaki, H. Sato and Y. Watanabe: Physica C 178 (1991) 339.

[21] T. Mori, A. Kobayashi, Y. Sasaki, H. Kobayashi, G. Saito and H. inokuchi: Bull. Chem. Soc. Jpn. 57 (1984) 627.

[22] For example; T. Sasaki, H. Sato and N. Toyota: Solid State Commun. 76 (1990) 507.

[23] M.V. Kartsovnik, A.E. Kovalev, V.N. Laukhin, H. Ito, T. Ishiguro, N.D. Kushch, H. Anzai and G. Saito: Synth. Metals, 70 (1995) 819.

[24] T. Komatsu, N. Matsukawa, T. Nakamura, H. Yamochi, G. Saito, H. Ito and T. Ishiguro: Phosphorus, Sulfer, and Silicon 67 (1992) 295.

[25] H. Anzai, J.M. Delrieu, S. Takasaki, S. Nakatsuji and J. Yamada: Synth. Metals, 70 (1995) 1115.

[26] J. Lawrence and S. Doniach: *Proc. 12th Int. Conf. on Low Temp. Phys.*, Kyoto 1970 (Academic Press of Japan, Tokyo, 1971)

[27] S. Hikami and A.I. Larkin: Mod. Phys. Lett. B2 (1988) 693.

[28] T. Tsuneto: J. Phys. Soc. Jpn. 57 (1988) 3499.

[29] R. Ikeda, T. Ohmi and T. Tsuneto: J. Phys. Soc. Jpn. 60 (1991) 1051.

[30] R. Ikeda and T. Tsuneto: J. Phys. Soc. Jpn. 60 (1991) 1337.

[31] B. Andraka, J.S. Kim, G.R. Stewart, K.D. Carlson, H.H. Wang and J.M. Williams: Phys. Rev. B40 (1989) 11345.

[32] J.E. Graebner, R.C. Haddon, S.V Chichester and S.H. Glarum: Physs. Rev. b41 (1990) 4808.

[33] B. Andraka, C.S. Jee, J.S. Kim, G.R. Stewart, K.D. Carlson, H.H. Wang, A.V.S. Crouch, A.M. Kini and J.M. Williams: Solid State Commun. 79 (1991) 57.

[34] Y. Watanabe, T. Sasaki, H. Sato and N. Toyota: J. Phys. Soc. Jpn. 61 (1991) 2118; Y. Watanabe, H. Sato, T. Sasaki and N. Toyota: J. Phys. Soc. Jpn. 61 (1991) 3608.

[35] W.K. Kwok, U. Welp, K.D. Carlson, G.W Crabtree, K.G. Vandevoort, H.H. Wang, A.M. Kini, J.M. Williams, D.L. Stupka, L.K. Montgomery and J.E. Thompson: Phys Rev. B42 (1990) 8686.

[36] K. Oshima, H. Urayama, H. Yamochi and G. Saito: J. Phys. Soc. Jpn. 57 (1988) 730.

[37] K. Murata, Y. Honda, H. Anzai, M. Tokumoto, K. Takahashi, N. Kinoshita, T. Ishiguro, N. Toyota, T. Sasaki and Y. Muto: Synth. Metals 27 (1988) A341.

[38] K. Oshima, H. Urayama, H. Yamochi and G. Saito: Synth. Metals 27 (1988) A473.

[39] M. Tokumoto, N. Kinoshita, Y. Tanaka and H. Anzai: J. Phys. Soc. Jpn. 60 (1991) 1426.

[40] S. Ullah and A.T. Dorsey: Phys. Rev. B44 (1991) 262.

[41] U. Welp, S. Fleshler, W.K. Kwok, R.A. Klemm, V.M. Vinokur, J. Downey, B. Veal and G.W Crabtree: Phys. Rev. Lett. 67 (1991) 3180.

[42] R. Ikeda, T. Ohmi and T. Tsuneto: JJAP Series 7 Mechanisms of Superconductivity 1992, pp.354.

[43] M. Lang, F Steglich, N. Toyota and T. Sasaki: Phys. Rev. B 49 (1994) 15227.

[44] A. Otsuka, T. Ban, G. Saito, H. Ito, T. Ishiguro, N. Hosoito and T. Shinjo: Synth. Metals 55-57 (1993) 3148.

[45] L.I. Buravov, V.N. Laukhin and A.G. Khomenko: Sov. Phys. JETP 61 (1985) 1292.

[46] V.B. Ginodman, A.V Gudenko, P.A. Kononovich, V.N. Laukhin and I.F. Shchegolev: Sov. Phys. JETP 67 (1988) 1055.

[47] T. Nakamura, T. Komatsu, G. Saito, T. Osada, S. Kagoshima, N. Miura, K. Kato, Y. Maruyama and K. Oshima: J. Phys. Soc. Jpn. 62 (1993) 4373.

[48] H. Sato, H. Taniguchi, Y. Nakazawa, A. Kawamoto, K. Kato and K. Kanoda: Synth. Metals 70 (1995) 915.

[49] R.Ikeda, T.Ohmi and T.Tsuneto, J. Phys. Soc. Jpn. 58 (1989) 1377.

[50] J. Bardeen and M.J. Stephan: Phys. Rev. 140 (1965) A1197.

[51] P.W Anderson and Y.B. Kim: Rev. Mod. Phys. 36 (1964) 39.

[52] M. Tinkham: Phys. Rev. Lett. 61 (1988) 1658.

[53] P.H. Kes, J. Aarts, J. van der Berg, C.J. van der Beek and J.A. Mydosh: Supercond. Sci. Technol. 1 (1989) 242.

[54] A. Umezawa, S.K. Malik, G.W Crabtree, H.H. Wang, L.K. Montgomery, K.D. Carlson and J.M. Williams: Physica C 185-189 (1991) 2665.

[55] V.V. Metlushko, V.D. Kuznetsov, L.A. Epanechnikov, E.F Markarov, E.B. Yagubskii and N.D. Kushch: Sov. Phys. JETP 74 (1992) 1041.

[56] K. Oshima, R.C. Yu, P.M. Chaikin, H. Urayama, H. Yamochi and G.Saito: *The Physics and Chemistry of Organic Superconductors* (Springer Verlag Berlin 1990), pp.276.

[57] F.L. Pratt, J. Caulfield, L. Cowey, J. Singleton, M. Doporto, W. Hayes, J.A.A.J. Perenboom, M. Kurmoo and P. Day: Synth. Metals 55-57 (1993) 2289.

[58] Y. Enomoto, K. Tanabe and A. Yamaji: Physica C 185-189 (1991) 1317.

[59] V Ambegaokar and B.I. Halperin: Phys. Rev. Lett. 22 (1969) 1364.

[60] G. Briceño, M.F. Crommie and A. Zettl: Phys. Rev. Lett. 66 (1991) 2164.

[61] K. Kadowaki, S.L. Yuan, K. Kishio, T. Kimura and K. Kitazawa: Phys. Rev. B50 (1994) 7230.

[62] S. Ravy, J.P. Pouget, C. Lenoir and P. Batail: Solid State Commun. 73 (1990) 37.

[63] K.E. Gray and D.H. Kim: Phys. Rev. Lett. 70 (1993) 1693.

[64] L.B. Ioffe, A.I. Larkin, A.A. Varlamov and L. Yu: Phys, Rev. B47 (1993) 8936.

[65] V.V. Dorin, R.A. Klemm, A.A. Varlamov, A.I. Buzdin and D.V. Livanov: Phys. Rev. 48 (1993) 12951.

[66] H. Ito, T.Ishiguro, K. Oka, Y. Nishihara: *Proc. of 7th International Symposium on Superconductivity, Kitakyushu, 1994*, in press.

[67] H. Fujii, K.Kajita, K. Kawada, Y. Nishio, H. Kobayashi, A. Kobayashi and R. Kato: Synth. Metals 55-57 (1993) 2939.

[68] T. Ishiguro, Yu.V. Sushko, H. Ito and G. Saito: J. Supercond. 7 (1994) 657.

[69] M.W. Coffey and J.R. Clem: Phys. Rev. Lett. 67 (1991) 386.

[70] M.W. Coffey and J.R. Clem: Phys. Rev. B45 (1992) 9872.

[71] K. Kanoda, K. Akiba, K. Suzuki and T. Takahashi: Phys. Rev. Lett. 65 (1990) 1271.

[72] M. Lang, N. Toyota, T. Sasaki and H. Sato: Phys. Rev. B 46 (1992) 5822.

[73] L.P Le, G.M.Luke, B.J. Sternlieb, W.D. Wu, Y.J. Uemura, J.H. Brewer, T.M. Riseman, C.E. Stronach, G. Saito, H. Yamochi, H.H. Wang, A.M. Kini, K.D. Carlson and J.M. Williams: Phys. Rev. Lett. 68 (1992) 1923.

[74] P.A. Mansky, P.M. Chaikin and R.C. Haddon: Phys. Rev. B 50 (1994) 15929.

[75] K. Kanoda, Y. Tsubokura, K. Ikeda, T. Takahashi, N. Matsukawa, G. Saito, H. Mori, B. Hilti and J.S. Zambounis: Synth. Metals 55-57 (1993) 2865.

[76] L.I. Glazman and A.E. Koshelev: Phys Rev. B43 (1991) 2835.

[77] J.R. Clem: Phys. Rev. B43 (1991) 7837.

[78] F. de la Cruz, H. Pastoriza, D. Lopez, M.F Goffman, A. Arribére and G. Nieva: Physica C 235-240 (1994) 83, and references therein.

[79] D. Lopez, G. Nieva and F de la Cruz: Phys. Rev. B50 (1994) 7219.